High performance core-shell Ni/Ni(OH)$_2$ electrospun nanofiber anodes for decoupled water splitting

Avigail Landman[a,†,*], Shabi Hadash[a,†], Gennady E. Shter[a], Hen Dotan[c], Avner Rothschild[b], and Gideon S. Grader[a,*]

[a] Department of Chemical Engineering, Technion – Israel Institute of Technology, Technion, Haifa, 3200003, Israel

[b] Department of Materials Science and Engineering, Technion – Israel Institute of Technology, Technion, Haifa, 3200003, Israel

[c] H2Pro, Ltd., Caesarea, Israel

[†] Equally contributed to this work

[*] Address correspondence to grader@technion.ac.il, slandman@technion.ac.il

Abstract

Decoupled water splitting has emerged as a promising new path for renewable hydrogen production, offering many potential advantages such as stable operation under partial-load conditions, high-pressure hydrogen production and overall system robustness. Here we demonstrate the performance of electrospun core-shell nickel/nickel hydroxide electrodes as redox anodes in an electrochemical – thermally activated chemical (E-TAC) decoupled water splitting process. The high surface area of the porous electrodes improves the charge capacity and current density of the redox anode while maintaining high process efficiency, reaching average current densities as high as 113 mA/cm^2 at an anode potential of 1.48 V$_{RHE}$ and 64 mA/cm^2 at 1.43 V$_{RHE}$, with a Faradaic efficiency of nearly 100% and no H$_2$/O$_2$ intermixing in a membraneless cell.

1. Introduction

Nickel hydroxide ($Ni(OH)_2$) is widely researched as an active material in electrodes for secondary alkaline batteries and pseudocapacitors owing to its favorable properties such as high theoretical capacity and reversible redox reactions.[1,2] There are countless techniques to prepare $Ni(OH)_2$ and $Ni(OH)_2$-based electrodes including electrochemical precipitation, or electrodeposition, of $Ni(OH)_2$ from a nickel salt solution onto a conductive substrate under cathodic polarization.[3,4] This is a facile and controllable synthesis method, and the electrodeposited $Ni(OH)_2$ layers possess large-area versatile morphologies.

Recently, we proposed electrodeposited $Ni(OH)_2$ anodes as solid redox anodes for decoupled water splitting in an electrochemical – thermally-activated chemical (E-TAC) cycle (Figure 1).[5,6] In this approach, the water splitting reaction is carried out in two temporally-separated steps. In the first step (Figure 1a), water is reduced at the cathode to produce hydrogen ($H_2O + e^- \rightarrow 1/2H_2 + OH^-$, $E^\theta = 0$ V_{RHE}, rxn. 1), while a $Ni(OH)_2$ anode is charged (oxidized) to NiOOH ($Ni(OH)_2 + OH^- \rightarrow NiOOH + H_2O + e^-$, $E^\theta \approx 1.4$ V_{RHE},[7,8] rxn. 2); E^θ is the standard potential of the respective reaction. The second step is a thermally-activated chemical step, wherein the charged NiOOH anode is heated in an alkaline solution (Figure 1b), promoting its spontaneous chemical reduction (regeneration) via reaction with water,[9] with concurrent oxygen evolution ($2NiOOH + H_2O \rightarrow 2Ni(OH)_2 + 1/2O_2$, rxn. 3):

Decoupled water splitting with solid redox anodes offers several potential advantages over conventional water electrolysis, including membraneless operation and a reduced risk of H_2/O_2 intermixing at high pressures and partial loads.[10,11] In addition, a key advantage of decoupled E-TAC water splitting is its high voltage efficiency compared to both conventional electrolysis and to other decoupling strategies.[6,12,13] This is due to the low potential of the $Ni(OH)_2$ oxidation reaction relative to that of the electrochemical oxygen evolution reaction (OER) that accompanies the hydrogen evolution reaction (HER) in conventional water splitting. Although the standard potential of the OER (1.23 V_{RHE}) is lower than that of the $Ni(OH)_2$/NiOOH couple (~1.4 V_{RHE}),[7,8] the four-electron OER is kinetically inhibited, with typical overpotential values ranging between 350 and 500 mV at a current density of 10 mA/cm^2.[14] By contrast, the one-electron $Ni(OH)_2$ charging reaction (rxn. 2) is kinetically facile, exhibiting much lower overpotentials at higher current densities. Furthermore, the reversible potential of $Ni(OH)_2$-based anodes may be lower than the standard value by several tens of mV depending on their structure and chemical composition.[15–17]

Despite their advantages, electrodeposited Ni(OH)$_2$ anodes still face several challenges. First, the nickel foams that typically serve as substrates for Ni(OH)$_2$ electrodeposition,[18–21] have relatively low surface areas, limiting the electrochemically active surface area of the deposited Ni(OH)$_2$ layer. Furthermore, adhesion and cracking issues can lead to performance deterioration, especially in dry conditions.[22] In the present study we propose a route to address these challenges by designing high-surface area, versatile and stable core-shell Ni/Ni(OH)$_2$ nanofiber anodes, and evaluate their performance in E-TAC water splitting.

The active Ni(OH)$_2$ shell is formed by galvanostatic cycling of a porous nanofiber nickel substrate prepared by electrospinning, a highly versatile technique for fabrication of polymeric, inorganic and hybrid nanomaterials with unique physical and chemical properties.[23] Recently, many studies have demonstrated core-shell nanostructures with electrospun carbon cores chemically coated with Ni(OH)$_2$ shells for supercapacitor applications.[24–27] Such nanostructures offer exceptional gravimetric charge capacity densities (a.k.a. specific capacities) due to the high ratio of electrochemically active surface area to the active material mass. However, due to their low active material loading, these structures are not compatible with the capacity requirement in E-TAC water splitting to achieve sufficiently long charging / hydrogen generation steps. Core-shell structures with metallic nickel cores have also been demonstrated, exhibiting exceptionally high rates and charge capacity densities normalized to the mass of the active material.[28–31] However, these electrodes also suffer from low capacity due to their low mass loadings.

Our present work demonstrates superior performance of core-shell Ni/Ni(OH)$_2$ nanofiber anodes with improved charge capacity and high rate capabilities based on several process metrics, and an enhanced performance towards E-TAC water splitting.

2. Experimental

2.1. Materials

Nickel and cobalt precursor solutions for electrospinning were prepared from ACS grade nickel and cobalt acetate tetrahydrate (Section S1.1, Supporting Information). Nickel and cobalt solutions for electrochemical deposition were prepared from analytical grade nickel and cobalt nitrate (Section S1.1, Supporting Information). All solutions were prepared from analytical grade solvents or de-ionized water. Alkaline solutions for electrochemical characterization were prepared using reagent grade potassium hydroxide flakes.

4

2.2 Ni(OH)₂ electrodeposited anode synthesis

Electrodeposited anodes (EDAs) were prepared as described elsewhere[6] (Section S2 and Figure S12, Supporting Information). Briefly, nickel foam (Ni-4753, RECEMAT, 95.2% porosity with 400 μm average pore size) was dipped in an aqueous solution of nickel nitrate and cobalt nitrate and subjected to galvanostatic cathodic polarization at a current density of 60 mA/cm^2 (normalized by the geometric area) for 1 h. After deposition, the anodes were aged in an aqueous solution of 5M KOH at 90°C for 30 min to convert the deposited α-Ni(OH)₂ phase to the stable β-Ni(OH)₂ phase.

2.3 Core-shell Ni/Ni(OH)₂ nanofiber anode synthesis

Firstly, nickel precursor solutions with and without cobalt precursor were electrospun, forming "green" nanofiber (NF) mats (Figures S1a and S2, Supporting Information). Secondly, the mats were calcined in air resulting with nickel oxide (NiO) (Figures S1b, S1c, and S3 Supporting Information). Then, the NiO mats were gently ground to form a coarse powder that was mixed with a polymer binder solution (Figures S1d, S1e, and S4 Supporting Information) and pressed, forming a NiO pellet. The NiO pellet was subsequently reduced under H₂/N₂ (5% : 95%) atmosphere to produce a porous nickel (Ni^0) substrate (Table S1, Supporting Information) comprising of highly porous nickel nanofibers (Figures S1f and S5, Supporting Information).

Prior to all layer growth procedures, the substrate was dipped in 5M KOH solution at 90°C for 2 h to promote initial growth of the desired phase (Figure S6, Supporting Information). To form an active Ni(OH)₂ surface layer, the porous nickel substrate was connected as the working electrode in a two-electrode configuration with a Ni foil counter electrode (15 cm^2) and subjected to galvanostatic cycling at a constant current density of ±200 mA/cm^2 (normalized by the geometric area of the working electrode) in an aqueous solution of 5M KOH at a temperature of 55 ± 5°C (Section S1.2.1, Supporting Information).

2.4 Materials characterization

The morphology and microstructure of nanofiber-based and electrodeposited anodes were investigated by high resolution SEM (HRSEM ULTRA plus, Zeiss, Zurich, Switzerland). Qualitative mapping and quantitative elemental analysis were carried out by EDS (Oxford SDD EDS). Verification of crystal phases was carried out by XRD (Smartlab 9kW Rigaku). Surface area and pore size distribution measurements were made using a FlowSorb III 2310 surface area analyzer (Micromeritics corporation, USA) through N₂ adsorption-desorption.

2.5 Electrochemical characterization and E-TAC water splitting tests

Electrochemical tests were carried out in a three-electrode system, with the NFA or EDA as the working electrode, platinum foil (1 cm^2) as the counter electrode, and an Hg/HgO/1M NaOH (RE-6, ALS Co., 0.118 V$_{SHE}$) as the reference electrode, using a multi-channel potentiostat (Ivium-n-stat, Ivium Technologies). The electrolyte for electrochemical measurements was an aqueous solution of 5M KOH at ambient temperature, and the electrolyte for chemical regeneration during E-TAC water splitting tests was 5M KOH at 95°C.

E-TAC water splitting tests were carried out by first charging the anode at a constant potential of 1.48 or 1.43 V$_{RHE}$ in 5M KOH solution at ambient temperature for a set duration of 100, 200, 400 or 800 s, and then regenerating the electrode by dipping it in a hot (95°C) 5M KOH solution for the same duration. Stability tests were carried out with 100 s charge/regeneration cycles (Section S1.2.2, Supporting Information). In addition, the anode was also subjected to E-TAC cycles with short regeneration times, wherein the charging duration varied between 100 and 800 s, but the regeneration duration was kept constant at 100 s (Section S3.1, Supporting Information).

3. Results and discussion

3.1 Phase and morphology characterization

Nickel (oxy)hydroxides exist in various crystalline forms, which are usually classified into four general phases: alpha- and beta-nickel hydroxides (α-Ni(OH)$_2$ and β-Ni(OH)$_2$, respectively), and beta- and gamma-nickel oxyhydroxides (β-NiOOH and γ-NiOOH, respectively).[32,33] The β-Ni(OH)$_2$ phase is crystalline, stable in alkaline conditions, and can be reversibly oxidized to the β-NiOOH phase according to the reaction: β-Ni(OH)$_2$ + OH$^-$ $\leftrightarrows$ β-NiOOH + H$_2$O + e$^-$.[3,33,34] The β-Ni(OH)$_2$/β-NiOOH couple has a remarkable cycling durability,[8,35] and a high theoretical charge capacity of 1040 C/g. However, overcharging the β-phase may result in the formation of the γ-NiOOH phase, which exhibits a much larger inter sheet distance, and therefore leads to swelling and consequently to fast deterioration of electrode performance upon cycling. Although α-Ni(OH)$_2$ may be directly charged to γ-NiOOH with a higher charge capacity (up to 1726 C/g), the α-phase is unstable in alkaline solutions and quickly transforms to the stable β-phase. For these reasons, nickel (oxy)hydroxide electrodes are best cycled in the β/β system by avoiding overcharging.

6

Metallic nickel (Ni^0) and its native oxide (NiO) can be electro-oxidized to α-Ni(OH)$_2$ in the potential range between 0 and 0.5 V_{RHE} in alkaline solutions. Upon application of more positive potentials, α-Ni(OH)$_2$ undergoes an irreversible transformation to β-Ni(OH)$_2$, which is then oxidized to β-NiOOH[36]. Medway *et al.* proposed that cycling over the Ni(OH)$_2$/NiOOH redox potential region results in thickness growth of both the Ni(OH)$_2$ and, to a lesser extent, of the underlying NiO layer. As the thickness of the layers increases, mass and charge transport impede further growth of the Ni(OH)$_2$ layer, and it reaches a stable thickness.[36–38] An alternative growth mechanism involving the dissolution of Ni^0 into Ni^{2+} followed by its immediate precipitation as Ni(OH)$_2$ has been recently suggested by Davydova *et al.*[39] Here, the nickel substrate was subjected to galvanostatic cycling between +200 and -200 mA/cm^2 in an aqueous solution of 5M KOH at a slightly elevated temperature of 55 ± 5°C to grow a substantial active layer. The weight of the electrode increased with cycling, reaching stabilization in weight gain and charge after roughly 30 cycles (Figure S7, Supporting Information). Figure 2 shows X-ray diffractograms of the NFA in different stages of preparation. Bragg reflections of metallic nickel were clearly observed in the porous nickel substrate before aging and active layer growth (light blue curve). After completing the layer growth process, Bragg reflections of the β-Ni(OH)$_2$ phase appeared (blue curve). The direct formation of the β-phase can be attributed to the oxidation conditions (high potential, temperature and KOH concentration), which are known to promote the aging process, wherein α-Ni(OH)$_2$ is converted to β-Ni(OH)$_2$.[3,33]

Figure 3 presents high-resolution SEM micrographs of the Ni/Ni(OH)$_2$ nanofibers before and after active layer growth. Prior to layer growth (Figure 3a), the nickel substrate comprised of short (up to ~1 µm) NF shreds with an average fiber diameter of ~250 nm, and a closely packed and highly porous structure. Based on volume and weight measurements, the relative density of the porous Ni NF substrate was 24.5-26.5%, reflecting an overall porosity of ~75%. Figure 3b presents the Ni/Ni(OH)$_2$ nanofibers after layer growth by galvanostatic cycling. The Ni(OH)$_2$ layer grew in a highly porous coral structure comprising of thin sheets, 20-50 nm in size, separated by 30-100 nm gaps. Based on the weight gain, approximately 30 mol% of the original nickel transformed to nickel hydroxide, resulting in a core-shell structure with Ni core and Ni(OH)$_2$ shell. The cobalt-doped Ni/Ni$_{0.9}$Co$_{0.1}$(OH)$_2$ NFAs were prepared similarly, by galvanostatic cycling of a cobalt-doped nickel substrate and presented a similar nanostructure (Figure S8, Supporting Information). Figure 4 shows EDS maps of the as-prepared NiCo fibers (10 wt.% cobalt, Table S2, Supporting Information), displaying a homogeneous distribution of cobalt within the nickel fibers.

BET measurements were carried out to evaluate the surface area of the NFA before and after layer growth (Figure 5). Prior to layer growth, the BET-nitrogen surface area of the as-prepared Ni NF substrate was 4.5 m^2/g (Figure 5a). For comparison, the surface area of the commercial nickel foam substrate used in the preparation of EDA samples was ~0.01 m^2/g (Section S2.2 and Figure S13, Supporting Information). The BET-nitrogen surface area increased significantly after layer growth, reaching 22.9 m^2/g. A bimodal mesopore size distribution was observed as shown in Figure 5b, with two peaks at pore diameters of approximately 3 and 30 nm before layer growth, and 3 and 16 nm after layer growth. Additionally, the total pore volume of small pores (with diameter < 100 nm) increased by a factor of 6.5 after $Ni(OH)_2$ layer growth. This can be attributed to the growth of the porous $Ni(OH)_2$ layer, as shown in Figure 3. Overall, a hierarchical meso/macro porous structure with a high surface area was obtained.

3.2. Electrochemical characterization of Ni/Ni(OH)$_2$ and Ni/Ni$_{0.9}$Co$_{0.1}$(OH)$_2$ nanofiber anodes

Core-shell electrospun nickel hydroxide electrodes were prepared to serve as redox anodes for decoupled E-TAC water splitting (Figure 1b). To characterize their electrochemical properties, the anodes were subjected to cyclic voltammetry (CV) scans. The CV scan of a Ni/Ni(OH)$_2$ NFA (Figure 6, red curve) displayed a single redox wave centered around 1.34 V_{RHE}, which provides a good approximation for the anode's reversible redox potential (E^0). The reversible potential is an important electrochemical property of Ni(OH)$_2$ anodes for E-TAC water splitting, as the cell voltage during the first (hydrogen generation) step is directly related to the Ni(OH)$_2$ oxidation potential according to: $V_{cell} = E_{anode} - E_{cathode} + \sum iR = (E^0_{anode\ rxn} + \eta_{anode}) - (E^0_{cathode\ rxn} - \eta_{cathode}) + \sum iR$ (eqn. 1); where V_{cell} is the cell voltage, E is the applied potential, E^0 is the reversible potential, $\eta = E - E^0$ is the overpotential and $\sum iR$ is the sum of all the series resistance Ohmic losses. Thus, a low anodic redox potential alongside a minimal anodic overpotential contribute to a high voltage efficiency (1.48/V_{cell}).

Additionally, since parasitic oxygen evolution may take place upon charging the anode to a high state of charge (SOC), a lower redox potential shifts the anode charging reaction away from the OER and enables charging the anode to higher SOCs without parasitic oxygen evolution.[40,41] To evaluate the OER rate at the NFAs, the anodes were subjected to chronoamperometric measurements between 1.43 and 1.48 V_{RHE} (Section S3.3 and Figure S20, Supporting Information). By allowing the current to stabilize, a distinction could be made between the pseudo-capacitive Ni(OH)$_2$ oxidation current and the steady-state OER Faradaic current. The corresponding steady-state Tafel plot for the OER Faradaic current at the Ni/Ni(OH)$_2$ NFA is plotted in Figure 6 (red circles). As can be seen, the onset potential for the OER at the

Ni/Ni(OH)$_2$ NFA (taken at j_{OER}=1 mA/cm^2 from the exponential fit) was 1.47 V$_{RHE}$, about 130 mV above the reversible redox potential of the Ni(OH)$_2$/NiOOH couple (1.34 V$_{RHE}$), and 30 mV above the peak of its oxidation wave (at a potential of 1.44 V$_{RHE}$). Thus, this anode can be oxidized at ambient conditions without concurrent oxygen evolution.

The reversible redox potential, as well as the charging and discharging overpotentials, are also affected by incorporation of various additives and dopants into the Ni(OH)$_2$ anode. Specifically, cobalt is known to shift the Ni(OH)$_2$ redox potentials cathodically and improve the electron and proton conductivity of Ni(OH)$_2$, allowing the anode to reach greater SOCs.[33,40,42] Here, cobalt was embedded into the electrospun fibers, and evenly dispersed along the fibers, as shown in Figure 4. The addition of cobalt resulted in a cathodic shift of the Ni(OH)$_2$/NiOOH reversible redox potential by 53 mV (Figure 6, blue curve). However, it also catalyzed the OER compared to the undoped anode, as shown by the steady-state Tafel plot in Figure 6 (blue circles). The OER onset potential at the cobalt doped NFA was around 1.43 V$_{RHE}$, lower than for the undoped anode. Table 1 summarizes the potential values derived from the CV scans and steady-state polarization tests of the doped and undoped anodes, including: Ni(OH)$_2$/NiOOH redox, oxidation and reduction potentials (E^0, E_{ox} and E_{red}, respectively), the OER onset potential (E_{onset}) and the potential difference between E_{ox} and E_{onset}.

2.3. Performance of cobalt-doped and undoped NF anodes in E-TAC water splitting

There are several key performance metrics in the selection and optimization of Ni(OH)$_2$ anodes for E-TAC water splitting. As discussed in the previous section, the first critical metric is the Ni(OH)$_2$ redox potential, which directly influences the cell voltage (see eqn. 1) and therefore the process' voltage efficiency. Here, the anodes' charging potential was controlled by applying a constant polarization potential of either 1.48 or 1.43 V$_{RHE}$ during the hydrogen generation step. The highest value, 1.48 V$_{RHE}$, was chosen since it is the thermoneutral water splitting voltage, *i.e.*, this is the anode potential required in order to achieve a voltage efficiency of 100%$_{HHV}$ during the hydrogen generation step, neglecting all other losses (see eqn. 1).

The second key metric is the anode's charge capacity, as anodes with higher charge capacities can sustain longer cycles, reducing the cycling frequency. In this respect, Ni(OH)$_2$ anodes for E-TAC water splitting are similar to battery electrodes, which also benefit from high charge capacities that extend their operation duration between recharges. Thus, similarly to battery electrodes, the Ni(OH)$_2$ anodes are expected to exhibit high energy densities normalized by the anode's volume and mass. To achieve this, a sufficiently

9

high mass loading is necessary, along with a high utilization efficiency of the active mass. It should be noted that, unlike battery electrodes, the $Ni(OH)_2$ anodes in E-TAC water splitting are regenerated in a chemical process, rather than an electrochemical one, and therefore the rate of their regeneration cannot be directly controlled. As a result, the charge that can be chemically regenerated, Q_{regen}, is often lower than the charge that can be extracted by electrochemical discharge (see Section S3.2.1 and Figure S18, Supporting Information); in electrochemical discharging, a preset electrochemical driving force or reaction rate is imposed by an external power source, whereas in chemical discharging the driving force and reaction rate decrease progressively as the NiOOH anode is discharged.[6,9] In addition, the chemical discharging (regeneration) reaction takes place at the electrode-electrolyte interface and is limited by the diffusion of OH^- ions into the active material. Thus, while a high mass loading may improve the electrochemical charge capacity, it may not contribute to, and perhaps even reduce, the chemically-regenerated capacity, especially when achieved by increasing the bulk volume at the expense of surface area.

The third key metric is the current density during the hydrogen generation step, which is proportional to the hydrogen production rate. In this respect, $Ni(OH)_2$ anodes should support operation under high current densities normalized by the geometric area, similarly to alkaline electrolyzers, which typically operate at $200 - 400$ mA/cm^2.[43] However, in contrast to electrolyzer anodes wherein the OER takes place at the surface of the otherwise inert electrocatalyst, the charging reaction during E-TAC water splitting involves an electrochemical transformation of the anode itself from $Ni(OH)_2$ to NiOOH. Since the $Ni(OH)_2$ mass loading must be sufficiently high to sustain large charge capacities, there is a trade-off between rate capabilities and charge capacity, similar to the trade-off observed in electrodes for supercapacitors.[44]

In each test, the average regenerated charge was calculated based on the current×time product, according to: $Q_{regen} = \int i(t) \cdot dt = <i> \cdot t$, (eqn. 2); where t is the time, $i(t)$ is the current as a function of time, and $<i>$ is the average current over the entire test duration (see Figures S14 and S15 in the Supporting Information for the current $vs.$ time curves). Accordingly, for the tests carried out at 100, 200, 400 and 800 s, the ratio between the average current (in A) and the regenerated charge (in A·s) is 100, 200, 400 and 800, respectively. Figure 7 shows the regenerated charge capacities and current densities of the undoped and cobalt-doped NFAs compared to a cobalt-doped EDA. The values are normalized by all the key metrics, namely, the anode's volume, geometric area, total weight and active layer weight. The results are shown for tests carried out with equal durations of charging and regeneration of 100 s (Figure 7a), 200 s (Figure

7b), 400 s (Figure 7c) and 800 s (Figure 7d). The maximum values in each category are summarized in Table 2. Cobalt doping of the NFA resulted in enhanced performance in all metrics, with a higher charge and current density even at the low charging potential of 1.43 V_{RHE} compared to both the undoped NFA and the cobalt-doped EDA.

At a charging potential of 1.48 V_{RHE} (full line data series in Figure 7), the regenerated charge capacity was higher for both the doped and undoped NFAs compared to the EDA in all categories, with the exception of a higher gravimetric charge capacity per unit mass of the active layer for the shortest test duration. However, as the test duration increased, the gravimetric charge capacity of the EDA fell short of the NFAs, suggesting a mass and/or charge transport limitation into the depth of the electrodeposited $Ni(OH)_2$ active layer. An opposite trend was observed for the NFAs, wherein the regenerated charge increased at longer test durations. This could be attributed to the high porosity of the $Ni(OH)_2$ layer, which enables facile mass transport and therefore enhances the rate of the diffusion-limited regeneration reaction.

Both the cobalt-doped and undoped NFAs displayed similar regenerated charge capacities at a charging potential of 1.48 V_{RHE}. It therefore appears that under these experimental conditions, the benefits of cobalt doping were lost. Furthermore, the extent of the OER is greater at this potential for the cobalt-doped NFA compared to the undoped NFA, as can be seen in Figure 6. Indeed, 1.48 V_{RHE} lies anodicaly of the oxidation waves of both samples, and above the OER onset potential of the cobalt-doped NFA (Figure 6). However, we hypothesize that the lower oxidation potential of the cobalt-doped NFA compared to the undoped NFA could enable extraction of a higher charge at lower potentials, increasing the voltage efficiency without compromising the Faradaic efficiency of the charging reaction. This was demonstrated by repeating the same tests for both samples at a charging potential of 1.43 V_{RHE} (Figure 7, dashed lines).

As expected, the charge that could be extracted from both NFAs at 1.43 V_{RHE} was lower than at 1.48 V_{RHE}. Nevertheless, while the undoped NFA's retained only 34 - 49% (depending on the test duration) of its charge compared to that at 1.48 V_{RHE}, the cobalt-doped NFA retained 54 - 57% of its charge under the same conditions. Moreover, the regenerated charge for the cobalt-doped NFA, even at the low charging potential of 1.43 V_{RHE}, surpassed that of the EDA when charged at 1.48 V_{RHE} (Figure 7a-d, green lines). This is a significant improvement in anode performance, as the cobalt-doped NFA enables more charge to pass during the hydrogen production step, *i.e.*, increased hydrogen production, at lower potentials that give rise to a higher voltage efficiency. In addition, as opposed to 1.48 V_{RHE}, charging at 1.43 V_{RHE} improves the charge acceptance and lowers the risk of parasitic oxygen evolution during anode charging,

as the OER reaction rate at this anode is negligible at 1.43 V_{RHE} (Figure 6). This was also demonstrated by dissolved oxygen measurements, as discussed below.

The high surface area of the hierarchical meso/macro porous structure of the NFAs resulted in a significant increase in the obtainable current density at each potential. Compared to the EDA, the average current densities of the undoped and cobalt-doped NFAs at 1.48 V_{RHE} were higher by up to 6.5 and 7.6 times, respectively. Furthermore, even at 1.43 V_{RHE}, the current densities of the NFAs were higher compared to the EDA when charged at 1.48 V_{RHE} (by up to 2.2 and 4 times for the undoped and doped NFAs, respectively). At both 1.48 and 1.43 V_{RHE} charging potentials, the cobalt-doped NFA achieved higher current densities compared to its undoped counterpart, which is attributed to the larger driving force, *i.e.*, a larger difference between the applied potential (1.48 V_{RHE}) and the anode's redox potential.

The voltage efficiency of the E-TAC water splitting process using our cobalt-doped NFA in a two-electrode configuration was also compared to our previously reported anode.[6] At a current density of 50 mA/cm^2 (normalized by the geometric area), the low charging potential of the cobalt-doped NFA resulted in an overall lower cell voltage, with an increase in average voltage efficiency from 98.7% to 100% (see Section S3.1 and Figure S17, Supporting Information).

The fourth key metric in E-TAC water splitting is the Faradaic efficiency of the Ni(OH)$_2$ charging reaction, $(1 - Q_{OER}/Q_{total}$, where Q_{OER} is the parasitic charge of the OER during the hydrogen generation step, and Q_{total} is the total charge passed during the hydrogen generation step). The Faradaic efficiency is influenced by the cycle duration, which is linked to the anode's SOC, as well as by the anode's charging potential and its relation to the OER onset potential at the same anode. Q_{OER} was calculated at each E-TAC water splitting test from the measured amount of dissolved oxygen (see Section S4, Supporting Information). At 1.48 V_{RHE} charging potential, the Faradaic efficiency of the cobalt-doped NFA was high for the short tests (99%±1% for the 100 s test and 98.5%±0.7% for the 200 s test), but it decreased with increasing test duration, *i.e.*, upon charging to higher SOCs, reaching 94%±3% for the 400 s test, and only 85%±2% for the 800 s test (see Figure S21a, Supporting Information). However, by lowering the charging potential to 1.43 V_{RHE}, the Faradaic efficiency for the cobalt-doped NFA increased, reaching 98%±2% at the longest (800 s) test (see Figure S21b, Supporting Information). This result was expected , as the oxygen evolution rate is negligible at this potential. In fact, the ratio between the steady-state OER rate (Figure 6) and the overall reaction rate during charging can be used to estimate the lower limit of the Faradaic efficiency (see Section S4.1 and Figure S22, Supporting Information). Thus, the combination of increased

surface area, porosity and cobalt doping significantly improves the anode's performance and allows operation at lower potentials with higher charge capacities and better rate capabilities. For example, a cobalt-doped NFA can withstand long cycles of 800 s charging and regeneration, at a potential lower by 50 mV (1.43 V_{RHE}) while supplying charge and current densities that are up to 4 times greater (depending on the normalization basis) compared to the cobalt-doped EDA, at a Faradaic efficiency of ~100%.

In addition to the current density during the hydrogen generation step of the E-TAC water splitting cycle, it is advantageous for the oxygen generation step to be faster than the hydrogen generation step. This way the *overall* hydrogen production throughput is maximized. The fifth key metric is therefore the regeneration reaction rate, or the charge that can be regenerated at a given regeneration time, which is correlated to the hydrogen production throughput. To examine the influence of the anode preparation method on the regeneration rate, the E-TAC water splitting tests were repeated with shorter regeneration steps of only 100 s (see Section S3.1, Supporting Information). For the EDA, decreasing the regeneration time resulted in a capacity drop of up to 31±14%. However, for the undoped and cobalt-doped NFAs, the capacity dropped by only 12±4% and 13±4%, respectively (see Figure S16, Supporting Information). The enhanced surface area and availability of active sites of the NFAs thus also facilitate higher chemical reaction rates, increasing the hydrogen production throughput without a substantial loss in capacity. For example, a two-fold increase in hydrogen production duration (from 100 s to 200 s) with the cobalt-doped NFA corresponds to an overall hydrogen production throughput increase of 33%, with a capacity loss of less than 4%.

Finally, a highly important performance metric is the anode's cycling stability. $Ni(OH)_2$ battery electrodes can withstand thousands of electrochemical charge-discharge cycles by avoiding overcharging, as discussed above. Moreover, we have previously shown that the electrochemical discharge (reduction) of NiOOH can be seamlessly replaced by chemical regeneration without damage or degradation of the anode's microstructure, phase composition or chemical composition.[6] Here, the cycling stability of an undoped NFA was demonstrated by subjecting it to a series of 100 E-TAC water splitting cycles (see Figure S9, Supporting Information). After about 20 cycles, both anodes displayed high stability up the 100th cycle (Q = 5.2±0.3C and Q = 1.8±0.2 C for the EDA and NFA, respectively), with similar X-ray diffraction pattern and morphology to those observed after layer growth by galvanic cycling (Figures S10 and S11, Supporting Information). This is a preliminary positive indication of the anode's cycling stability

in E-TAC water splitting. A more extensive stability testing, which is typically carried out over thousands of cycles, is beyond the scope of this work.

2.4 Anode optimization: effect of fiber morphology

The electrochemical properties of a core-shell $Ni/Ni(OH)_2$ NFA depend on the microstructure and surface area of the nickel substrate. Tuning the anode's microstructure and consequent electrochemical performance is possible by controlling the various synthesis process parameters. To demonstrate this, we explored the influence of the fiber microporosity and diameter on the charge density of the resulting anodes. SEM images of three nickel nanofiber substrates prepared with maximum sintering temperatures of 500, 600, and 700°C are shown in Figures 8a, b, and c, respectively. The sintering temperature affects the fiber micro-structure and porosity, with almost complete loss of microporosity after sintering at 700°C, leaving only a very coarse granular microstructure. Preliminary electrochemical performance was then evaluated by electrochemical charge-discharge cycles (See Section S3.2.2, Supporting Information), showing a three-fold increase in volumetric charge capacity for the anode sintered at 500°C compared to 700°C (see Figure S19a, Supporting Information), presenting a clear advantage for maintaining a fine porous structure by controlling the sintering temperature.

Next, we looked at the fiber diameter, and its effect on the anode's performance. We postulated that reducing the fiber diameter would contribute to enhanced performance both by increasing the active surface area, and by increasing the weight ratio of the active shell layer and the nickel core. Thinning the fiber diameter was achieved by diluting the original precursor solution, so that its viscosity decreased twofold, and by raising the voltage during the ES process, which resulted in extra stretching of the fibers during electrospinning. Figure 8d shows the SEM images of a nickel nanofiber substrate having a fiber diameter of ~130 nm . The preliminary electrochemical performance demonstrates that reducing the fiber diameter by half results in almost doubling of the volumetric charge capacity (see Figure S19b, Supporting Information).

3. Conclusions

This work demonstrates stable and highly efficient E-TAC water splitting using core-shell $Ni/Ni(OH)_2$ nanofiber anodes prepared by electrospinning. The porous hierarchical structure that is achieved by this process enables to perform E-TAC water splitting at relatively high current densities with enhanced charge

capacities compared to electrodeposited $Ni(OH)_2$ anodes. Notably, the E-TAC water splitting system operates as a hybrid between a continuous electrolyzer, a high-capacity pseudocapacitor and a battery.[44] On the one hand, hydrogen production must be carried out at high rates, as in electrolyzers. To match benchmark values in this respect, the anode charging rate must be comparable to electrolysis reaction rates, which are standardized by the geometric area-normalized current densities (in mA/cm^2_{geo}). $Ni(OH)_2$ electrodes having high rate capabilities have been widely researched for pseudocapacitor applications. Such electrodes can withstand exceptionally high charge/discharge rates, usually in the range of 1-100 A/g.[28,30,31] Nevertheless, while such electrodes excel in active material-normalized gravimetric current and charge densities, their low active mass renders them unsuitable for our proposed application as redox anodes, which must excel in all metrics (volumetric, geometric and total gravimetric densities), in both current and charge. In this regard, our anodes are similar to battery electrodes, which require high capacities. While the rate capabilities of battery electrodes are limited, we have achieved high rate capabilities through an enhanced surface substrate. This work thus demonstrates an anode synthesis route by which the anode structure can be optimized for decoupled, high-rate and high-efficiency hydrogen production, displaying superior performance to electrodeposited anodes in all three metrics: geometric, gravimetric and volumetric.

Author contributions

Avigail Landman: Conceptualization, methodology, formal analysis, investigation, writing – original draft, visualization. **Shabi Hadash:** Investigation, validation, formal analysis. **Gennady E. Shter:** Methodology, supervision, project administration. **Hen Dotan:** Methodology, consultation. **Avner Rothschild:** Supervision, funding acquisition, writing – review & editing. **Gideon S. Grader:** Conceptualization, supervision, funding acquisition, project administration, writing – review & editing.

Acknowledgments

acknowledge Ziv Arzi for assisting in sample preparation and Alon Ben-Azaria and for assisting with DO testing.

Declaration of interests

References

1. Chen, J., Bradhurst, D. H., Dou, S. X. & Liu, H. K. Nickel hydroxide as an active material for the positive electrode in rechargeable alkaline batteries. *J. Electrochem. Soc.* **146**, 3606 (1999).

2. Wang, G., Zhang, L. & Zhang, J. A review of electrode materials for electrochemical supercapacitors. *Chem. Soc. Rev.* **41**, 797–828 (2012).

3. Hall, D. S., Lockwood, D. J., Bock, C., Macdougall, B. R. & Lockwood, D. J. Nickel Hydroxides and Related Materials : a Review of Their Structures , Synthesis and Properties. *Proc. R. Soc.* **471**, (2014).

4. Johnson, B. A., Ferro, R. E., Swain, G. M. & Tatarchuk, B. T. High surface Area , low-weight composite nickel fiber electrodes. *J. Power Sources* **47**, 251–259 (1994).

5. Rothschild, A., Grader, G., Shter, G., Landman, A. & Dotan, H. Methods and system for hydrogen production by water electrolysis. (2019).

6. Dotan, H. *et al.* Decoupled hydrogen and oxygen evolution by a two-step electrochemical– chemical cycle for efficient overall water splitting. *Nat. Energy* **4**, 786–795 (2019).

7. Bratch, S. G. Standard electrode potentials and temperature coefficients in water at 298.15K. *J. Phys. Chem. Ref. Data* **18**, 1–21 (1989).

8. Macdonald, D. D. & Challingsworth, M. L. Thermodynamics of nickel-cadmium and nickel-hydrogen batteries. *J. Electrochem. Soc.* **140**, 606–609 (1993).

9. Winsel, A. & Fischer, C. New apparatus for the measurement of the self-discharge of the nickel hydroxide electrode. *J. Power Sources* **34**, 331–338 (1991).

10. Liu, X., Chi, J., Dong, B. & Sun, Y. Recent Progress in Decoupled H2 and O2 Production from Electrolytic Water Splitting. *ChemElectroChem* **6**, 2157–2166 (2019).

11. Chisholm, G., Cronin, L. & Symes, M. D. Decoupled electrolysis using a silicotungstic acid electron-coupled-proton buffer in a proton exchange membrane cell. *Electrochim. Acta* **331**, 135255 (2020).

12. Symes, M. D. & Cronin, L. Decoupling hydrogen and oxygen evolution during electrolytic water splitting using an electron-coupled-proton buffer. *Nat. Chem.* **5**, 403–409 (2013).

13. Rausch, B., Symes, M. D., Chisholm, G. & Cronin, L. Decoupled catalytic hydrogen evolution from a molecular metal oxide redox mediator in water splitting. *Science (80-.).* **345**, 1326–1330 (2014).

14. Mccrory, C. C. L., Jung, S., Peters, J. C. & Jaramillo, T. F. Benchmarking Heterogeneous Electrocatalysts for the Oxygen Evolution Reaction. *J. Am. Chem. Soc.* **135**, 16977–16987 (2013).

15. Barnard, R., Randell, C. F. & Tye, F. L. Studies concerning charged nickel hydroxide electrodes . I. measurement of reversible potentials. *J. Appl. Electrochem.* **10**, 109–125 (1980).

16. Lee, S., Bai, L. & Hu, X. Deciphering Iron-Dependent Activity in Oxygen Evolution Catalyzed by Nickel–Iron Layered Double Hydroxide. *Angew. Chemie - Int. Ed.* **59**, 8072–8077 (2020).

17. Nguyen, T., Boudard, M., Carmezim, M. J. & Montemor, M. F. Layered Ni(OH)2-Co(OH)2 films prepared by electrodeposition as charge storage electrodes for hybrid supercapacitors. *Sci. Rep.* **7**, 1–10 (2017).

18. Li, M. *et al.* NiFe layered double hydroxide electrodeposited on Ni foam coated with reduced graphene oxide for high-performance supercapacitors. *Electrochim. Acta* **302**, 1–9 (2019).

19. Wang, Y. *et al.* Facile construction of Co(OH)2@Ni(OH)2 core-shell nanosheets on nickel foam as three dimensional free-standing electrode for supercapacitors. *Electrochim. Acta* **293**, 40–46 (2019).

20. Shahrokhian, S., Rahimi, S. & Mohammadi, R. Nickel-cobalt layered double hydroxide ultrathin nanosheets coated on reduced graphene oxide nonosheets/nickel foam for high performance asymmetric supercapacitors. *Int. J. Hydrogen Energy* **43**, 2256–2267 (2018).

21. Yang, G. W., Xu, C. L. & Li, H. L. Electrodeposited nickel hydroxide on nickel foam with ultrahigh capacitance. *Chem. Commun.* 6537–6539 (2008). doi:10.1039/b815647f

22. Hall, D. S., Lockwood, D. J., Poirier, S., Bock, C. & MacDougall, B. R. Raman and infrared spectroscopy of α and β phases of thin nickel hydroxide films electrochemically formed on nickel.

J. Phys. Chem. A **116**, 6771–6784 (2012).

23.   Jung, J.-W., Lee, C.-L., Yu, S. & Kim, I.-D. Electrospun nanofibers as a platform for advanced secondary batteries: a comprehensive review. *J. Mater. Chem. A* **4**, 703–750 (2016).

24.   Zhou, D. *et al.* 3D interconnected networks of ternary hierarchical carbon nanofiber/MnO2/Ni(OH)2 architecture as integrated electrodes for all-solid-state supercapacitors. *RSC Adv.* **6**, 71882–71892 (2016).

25.   Zhang, L. *et al.* Flexible Hybrid Membranes with Ni(OH)2 Nanoplatelets Vertically Grown on Electrospun Carbon Nano fi bers for High-Performance Supercapacitors. *ACS Appl. Mater. Interfaces* **7**, 22669–22677 (2015).

26.   Tian, D., Lu, X., Nie, G., Gao, M. & Wang, C. Direct growth of Ni-Mn-O nanosheets on flexible electrospun carbon nanofibers for high performance supercapacitor applications. *Inorg. Chem. Front.* **5**, 635–642 (2018).

27.   Ding, Q., Liu, M., Miao, Y., Huang, Y. & Liu, T. Electrospun nickel-decorated carbon nanofiber membranes as efficient electrocatalysts for hydrogen evolution reaction. *Electrochim. Acta* **159**, 1–7 (2015).

28.   Urso, M., Torrisi, G., Boninelli, S., Bongiorno, C. & Priolo, F. Ni(OH)2@Ni core-shell nanochains as low-cost high-rate performance electrode for energy storage applications. *Sci. Rep.* **9**, 1–11 (2019).

29.   Li, Q., Liang, C.-L., Lu, X.-F., Tong, Y.-X. & Li, G.-R. Ni@NiO core-shell nanoparticle tube arrays with enhanced supercapacitor performance. *J. Mater. Chem. A* **3**, 6432–6439 (2015).

30.   Dai, X. *et al.* Ni(OH)2/NiO/Ni composite nanotube arrays for high-performance supercapacitors. *Electrochim. Acta* **154**, 128–135 (2015).

31.   Xu, L., Zhang, L., Cheng, B. & Yu, J. Rationally designed hierarchical NiCo2O4-C@Ni(OH)2 core-shell nanofibers for high performance supercapacitors. *Carbon N. Y.* **152**, 652–660 (2019).

32.   Bode, H., Witte, J. & Dehmelt, K. Zur kenntnis der nickelhydroxidelektrode-I. uber das nickel (II)-hydroxidhydrat. *Electrochim. Acta* **11**, 1079–1087 (1966).

33.   Oliva, P., Laurent, J. F. & Leonardi, J. Review of the structure and the electrochemistry of nickel

hydroxides and oxy-hydroxides. *J. Power Sources* **8**, 229–255 (1982).

34.   Mcbreen, J. Nickel hydroxide. in *Handbook of battery materials* (eds. Daniel, C. & Besenhard, J. O.) 149–168 (Wiley-VCH Verlag GmbH & Co, 2011).

35.   Coates, D., Fox, C. & Miller, L. Hydrogen-based rechargeable battery systems: Military, aerospace, and terrestrial applications—I. Nickel-hydrogen batteries. *Int. J. Hydrogen Energy* **19**, 743–750 (1994).

36.   Medway, S. L. & Lucas, C. A. In situ studies of the oxidation of nickel electrodes in alkaline solution. *J. Electroanal. Chem.* **587**, 172–181 (2006).

37.   Hopper, M. A. & Ord, J. L. An Optical Study of the Growth and Oxidation of Nickel Hydroxide Films. *J. Electrochem. Soc.* **120**, 183–187 (1973).

38.   Seghiouer, A., Chevalet, J., Barhoun, A. & Lantelme, F. Electrochemical oxidation of nickel in alkaline solutions : a voltammetric study and modelling. *J. Electroanal. Chem.* **442**, 113–123 (1998).

39.   Davydova, E. S., Speck, F. D., Paul, M. T. Y., Dekel, D. R. & Cherevko, S. Stability Limits of Ni-Based Hydrogen Oxidation Electrocatalysts for Anion Exchange Membrane Fuel Cells. *ACS Catal.* **9**, 6837–6845 (2019).

40.   Wang, X., Luo, H., Yang, H., Sebastian, P. J. & Gamboa, S. A. Oxygen Catalytic Evolution Reaction on Nickel Hydroxide Electrode Modified by Electroless Cobalt Coating. *Int. J. Hydrogen Energy* **29**, 967–972 (2004).

41.   Snook, G. a., Duffy, N. W. & Pandolfo, A. G. Evaluation of the effects of oxygen evolution on the capacity and cycle life of nickel hydroxide electrode materials. *J. Power Sources* **168**, 513–521 (2007).

42.   Ortiz, M. G., Castro, E. B. & Real, S. G. Effect of cobalt electroless deposition on nickel hydroxide electrodes. *Int. J. Hydrogen Energy* **39**, 6006–6012 (2014).

43.   Smolinka, T., Ojong, E. T. & Garche, J. Hydrogen production from renewable energies - electrolyzer technologies. *Electrochem. Energy Storage Renew. Sources Grid Balanc.* 103–128 (2014). doi:10.1016/B978-0-444-62616-5.00008-5

44.   Simon, P., Gogotsi, Y. & Dunn, B. Where do batteries end and supercapacitors begin? *Science (80-.).* **343**, 1210–1211 (2014).
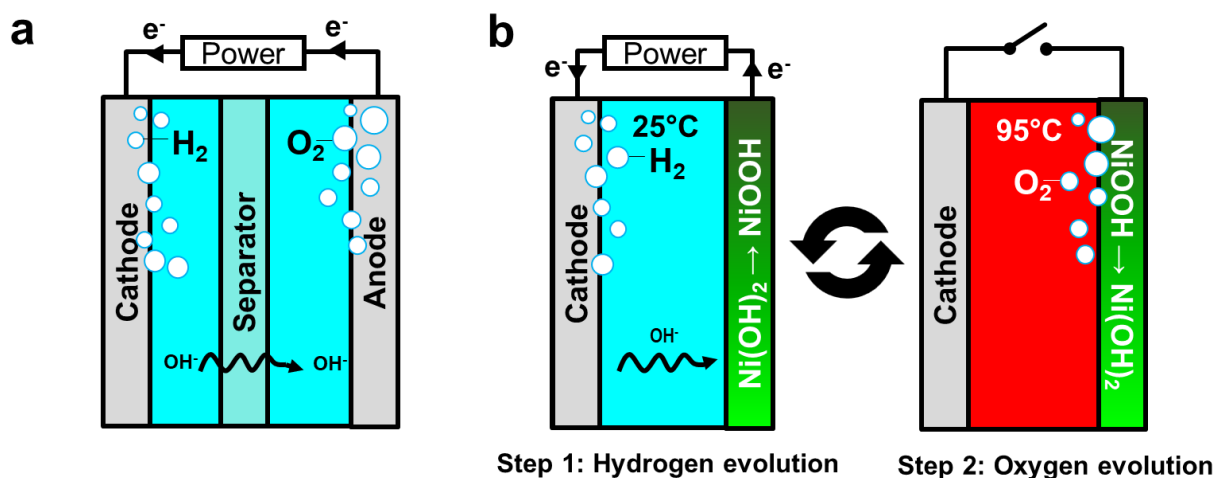
Figure 1: **Schematic illustration of conventional water splitting (a) and electrochemical – thermally-activated chemical (E-TAC) decoupled water splitting (b).** In conventional water splitting (alkaline electrolysis, a), the hydrogen and oxygen evolution reactions occur simultanously at the cathode and anode, respectively. A separator (membrane/diaphragm) is used to prevent H_2/O_2 intermixing. In E-TAC water splitting hydrogen and oxygen evolve in two separate steps (b). First, hydrogen evolution takes place at the cathode while the $Ni(OH)_2$ anode is electrochemically oxidized (charged) to NiOOH (Step 1: Hydrogen evolution). This step is carried out at ambient temperature (~25°C). Then, the cell is exposed to a hot (~95°C) electrolyte at open circuit, and oxygen is evolved as the NiOOH anode is chemically reduced back to $Ni(OH)_2$ (Step 2: Oxygen evolution). Both steps occur in alkaline electrolyte.
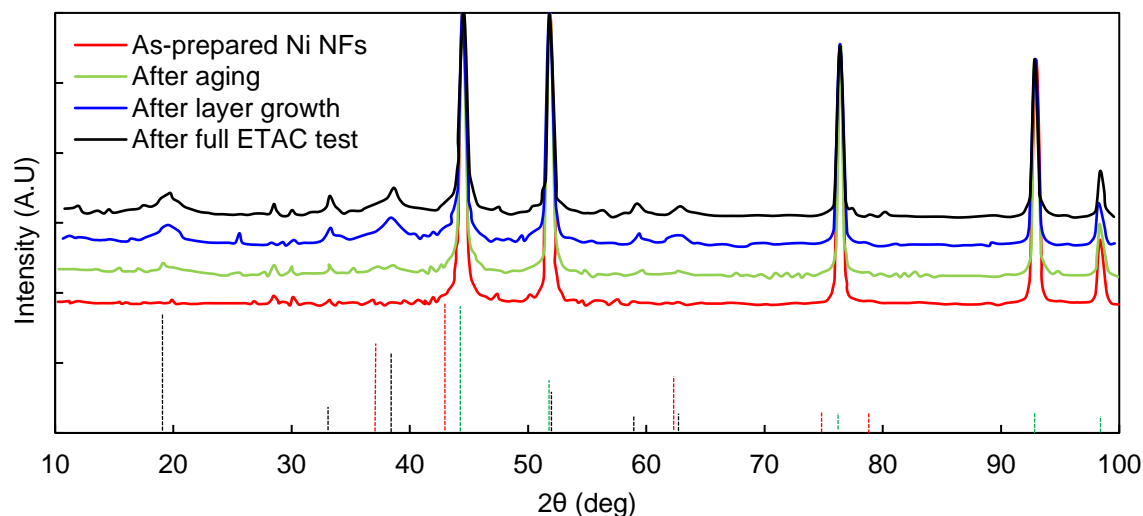
Figure 2: **X-ray diffractograms of a Ni/Ni(OH)₂ nanofiber anodes.** Diffractograms of a $Ni/Ni(OH)_2$ NFA formed by galvanostatic cycling after different preparation stages**:** as-prepared NF nickel substrate (red line); after aging for 2 h in 5M KOH at 90°C (green line); after active layer growth by galvanostatic cycling at 55°C (blue line); and after final characterization in a full E-TAC water splitting test (black line). The dashed vertical lines indicate the position and relative intensities of Bragg reflections of metallic nickel (JCPDS 00-004-0850, green), NiO (JCPDS 01-071-4750, red) and β-$Ni(OH)_2$ (JCPDS 00-059-0462, black).
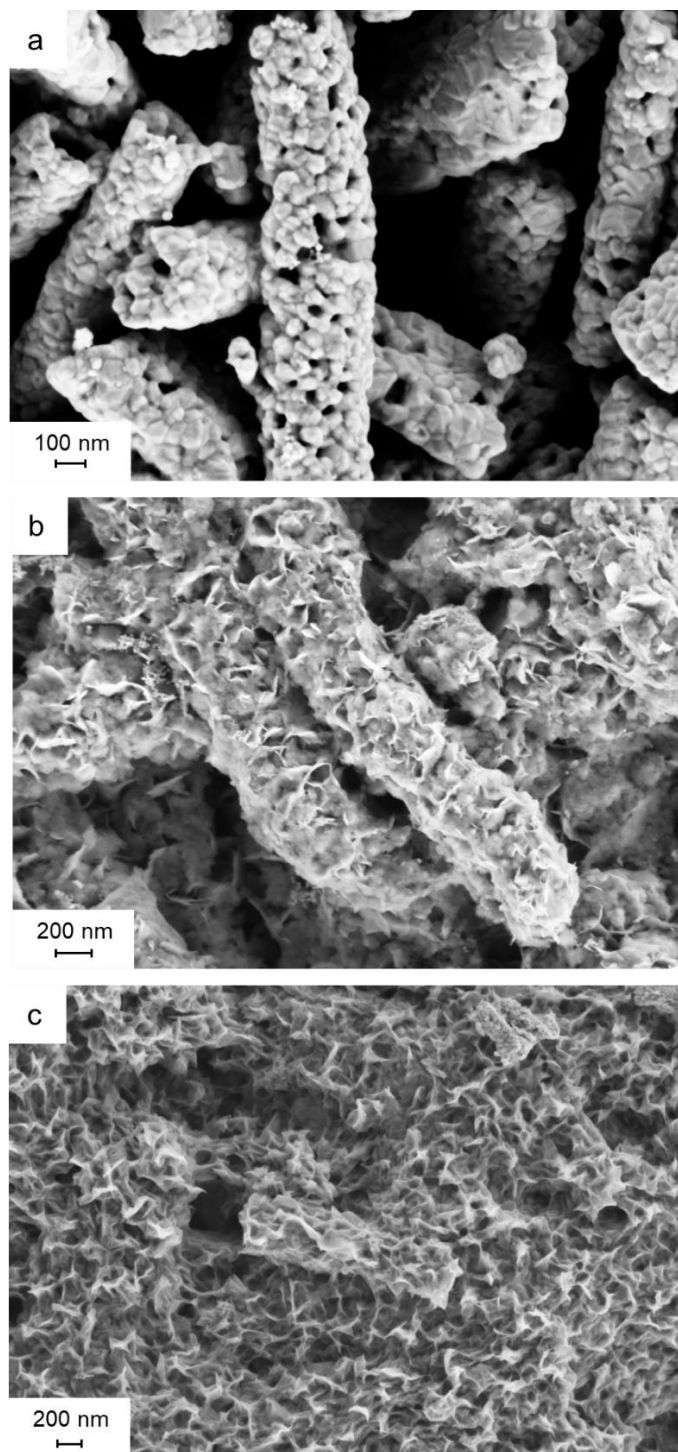
Figure 3: **HRSEM images of undoped Ni/Ni(OH)$_2$ nanofiber anodes.** (a) As-prepared Ni nanofiber substrate. (b) Ni/Ni(OH)$_2$ nanofiber anode after layer growth by galvanostatic cycling. (c) Ni/Ni(OH)$_2$ anode after E-TAC water splitting tests.
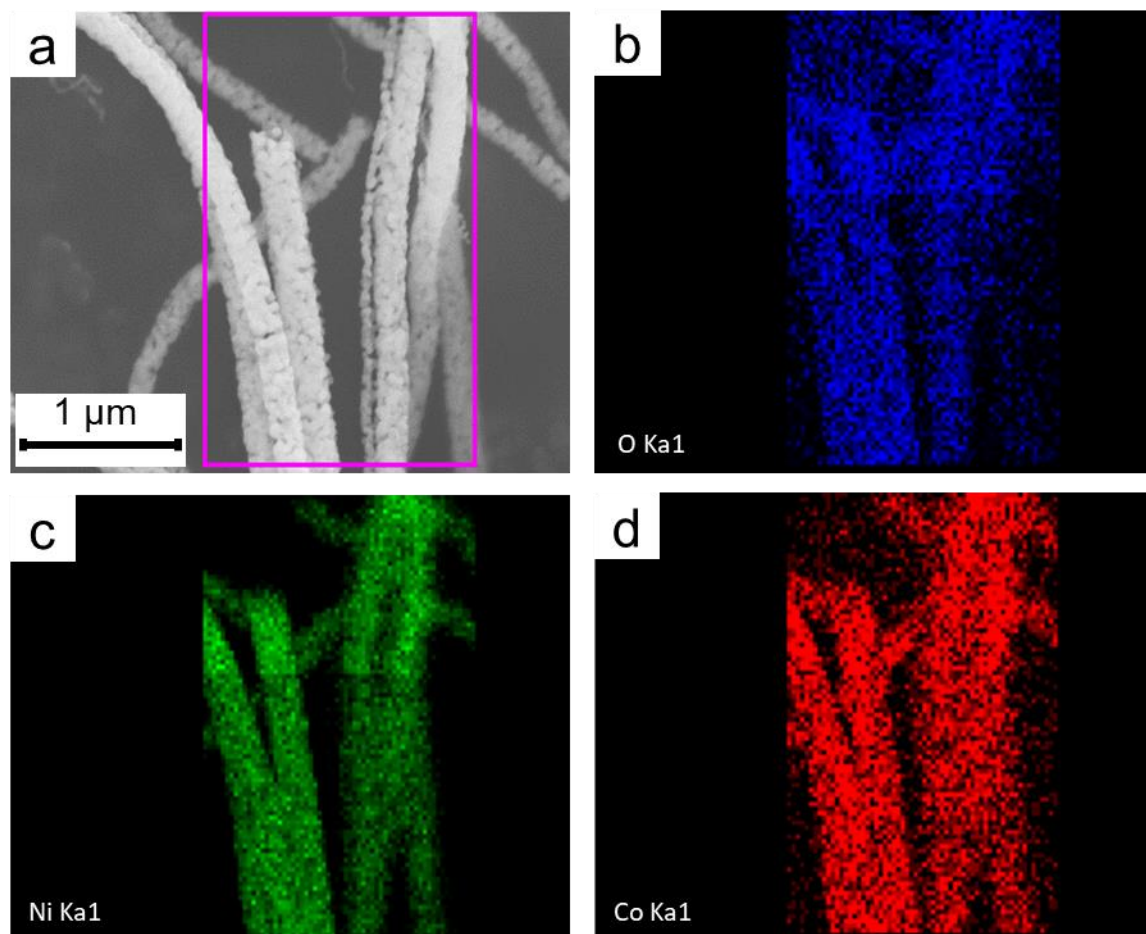
Figure 4: **Elemental distribution in a cobalt-doped nanofiber anode.** HRSEM micrograph (a) and the corresponding qualitative EDS mapping (b-c) of a cobalt-doped $Ni/Ni_{0.9}Co_{0.1}(OH)_2$ nanofiber anode prepared by galvanostatic cycling.
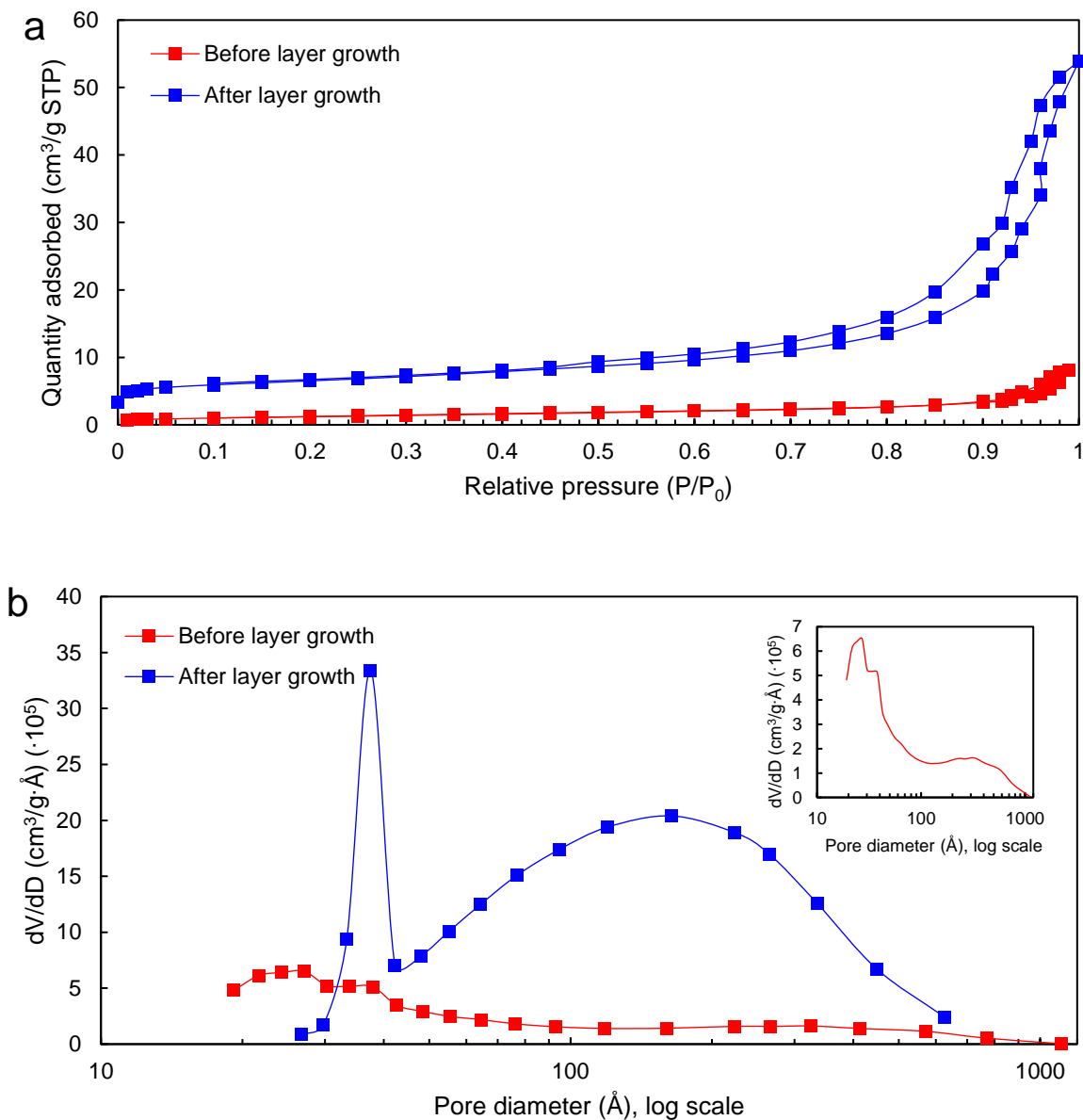
Figure 5: **Surface area and pore size distribution of a Ni/Ni(OH)$_2$ nanofiber anode.** (a) B.E.T N$_2$-absorption isotherms before and after Ni(OH)$_2$ active layer growth on a nanofiber nickel substrate (red and blue curves, respectively). (b) B.J.H N$_2$-desorption pore volume distribution before and after Ni(OH)$_2$ active layer growth by galvanostatic cycling. The inset shows the B.J.H plot before layer growth.
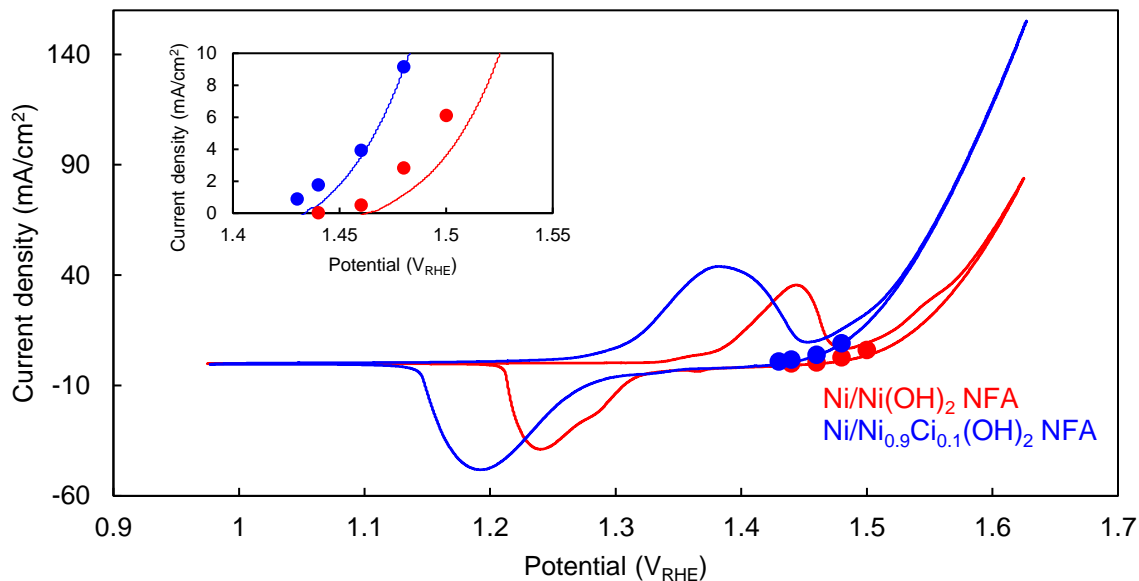
Figure 6: **Cyclic voltammograms of Ni/Ni(OH)$_2$ nanofiber anodes with and without cobalt**. CVs of an undoped Ni/Ni(OH)$_2$ NFA (red) and a cobalt-doped Ni/Ni$_{0.9}$Co$_{0.1}$(OH)$_2$ NFA (blue) measured at a scan rate of 0.05 mV/s. The red and blue circle data series represent the steady-state Tafel plots for the undoped and doped NFAs respectively. All tests were carried out in an aqueous solution of 5M KOH at ambient temperature. The inset shows a magnification of the steady-state Tafel area.
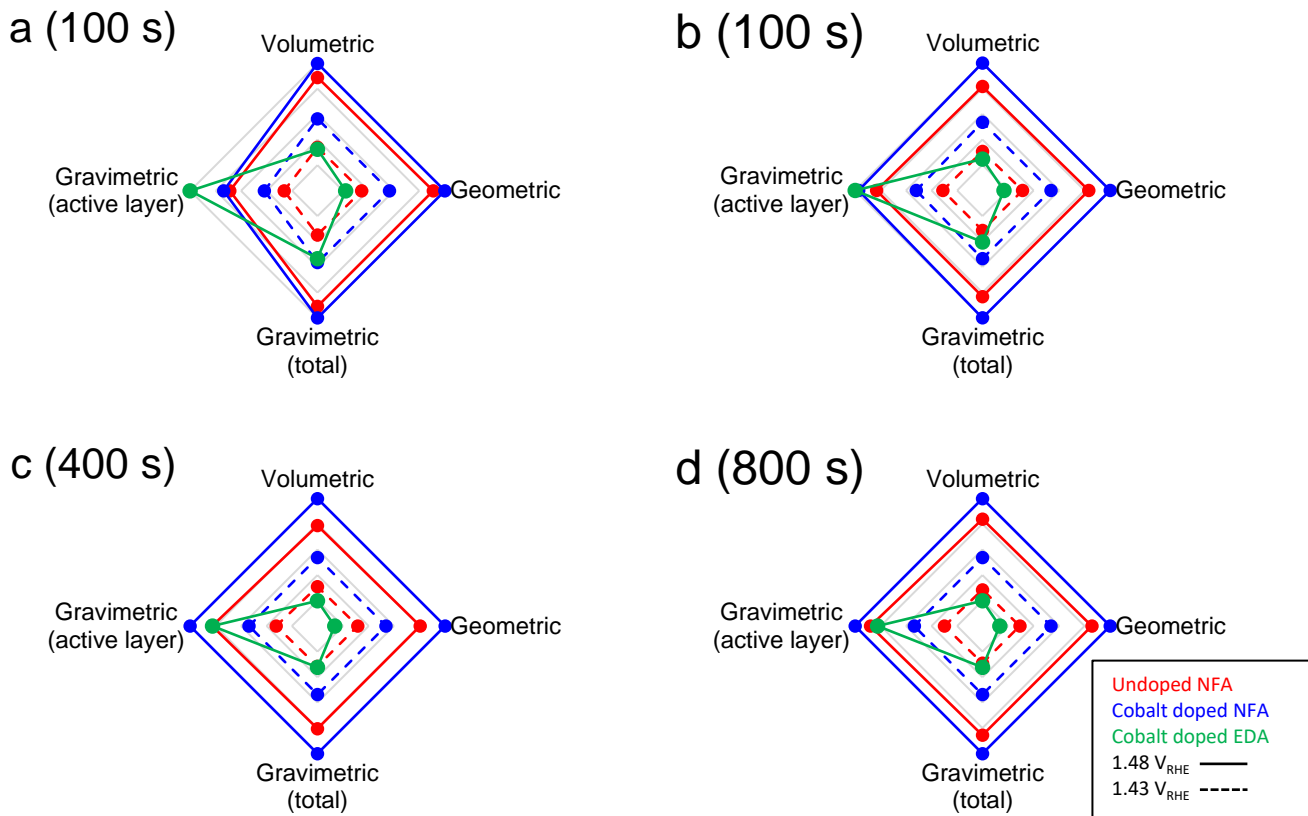
Figure 7: **Comparison of the regenerated charge and current density of an undoped Ni/Ni(OH)$_2$ nanofiber anode (red lines), a doped Ni/Ni$_{0.9}$Co$_{0.1}$(OH)$_2$ nanofiber anode (blue lines), and a doped Ni$_{0.9}$Co$_{0.1}$(OH)$_2$ electrodeposited anode (green lines) in E-TAC water splitting tests.** Charging was carried out by applying a constant potential of 1.48 V$_{RHE}$ (full lines) or 1.43 V$_{RHE}$ (dashed lines) in 5M KOH aqueous solution at ambient temperature for a set duration, and regeneration was carried out by dipping the charged anode in 5M KOH aqueous solution at 95°C for the same duration. The comparison is shown on the basis of the anode's volume, geometric area, total weight and active layer weight for E-TAC water splitting tests with charging / regeneration durations of 100 s (a), 200 s (b), 400 s (c) and 800 s (d). In each plot, all values are normalized by the highest values in that category, which are listed in Table 2. The center and circumference of each square represent relative values of 0% and 100%, respectively, and the inner gridlines are spaced at 20% intervals.
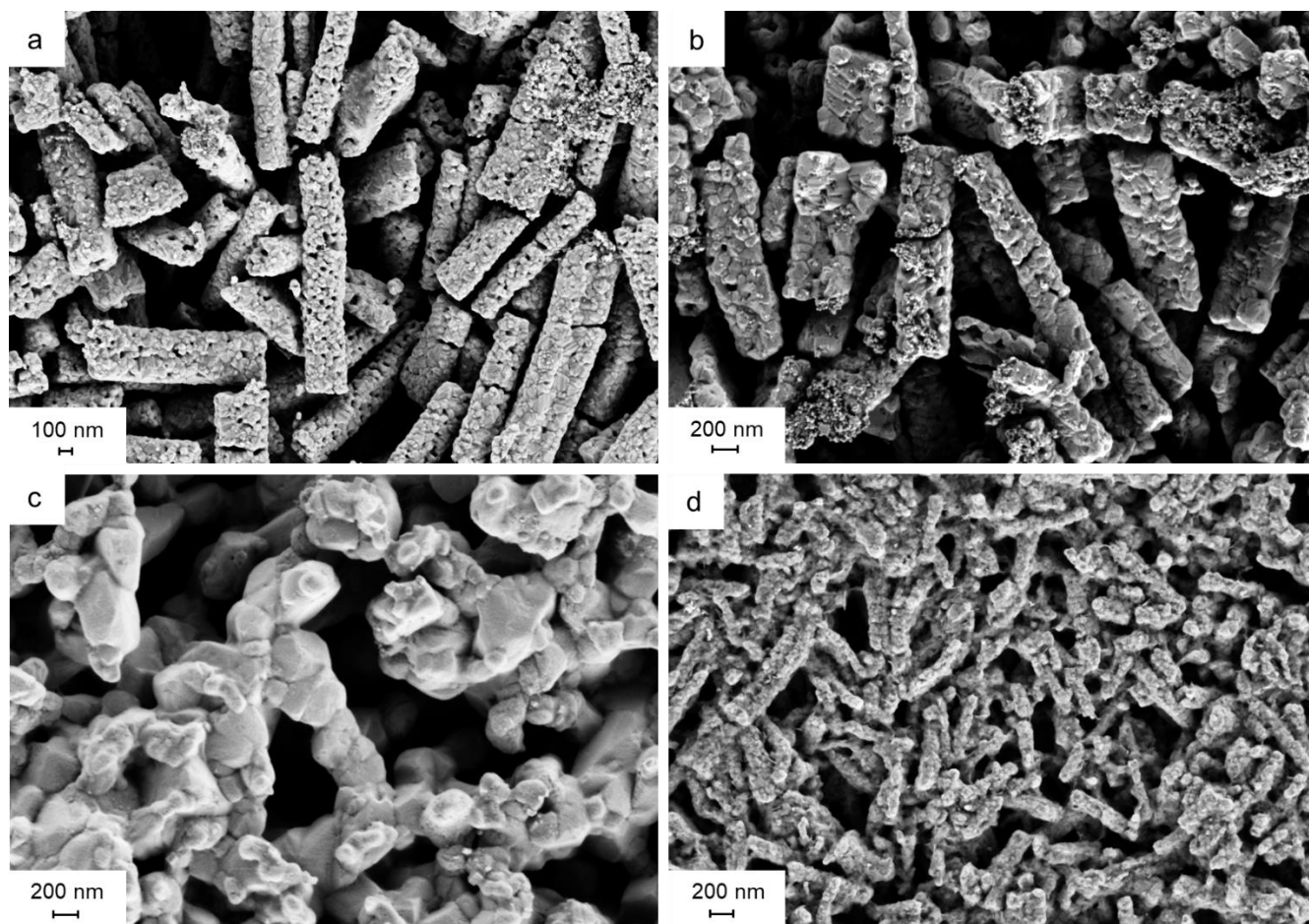
Figure 8: **Effect of temperatures parameters on NFE microstructure .** HRSEM images of nickel nanofiber anodes prepared at an ES voltage of 14 kVs with various maximum sintering temperatures of 500°C (a), 600°C (b) and 700°C (c), and at 500°C with a higher ES voltage of 26 kVs (d).

Table 1: **Summary of key electrochemical parameters.** Electrochemical parameters extracted from the cyclic voltammograms and steady-state polarization tests of $Ni/Ni(OH)_2$ and $Ni/Ni_{0.9}Co_{0.1}(OH)_2$ NFAs shown in Figure 8.

	E_{ox} (V_{RHE})	E_{red} (V_{RHE})	E^0 (V_{RHE})	E_{onset} (V_{RHE})	E_{onset} - E_{ox} (mV)
$Ni/Ni(OH)_2$ NFA	1.45	1.24	1.345	1.5	50
$Ni/Ni_{0.9}Co_{0.1}(OH)_2$ NFA	1.39	1.2	1.295	1.46	70

Table 2: **The maximum charging current density (j) and regenerated charge (Q) obtained in E-TAC water splitting tests with charging / regeneration durations of 100 s (a), 200 s (b), 400 s (c) and 800 s (d)**. The categories (a-d) correspond to figures 8a-8d, and the color coding corresponds to Figure 8 with values for the undoped NFA, cobalt doped NFA, and EDA marked in blue, red, and green, respectively.

Maximum Values	a (100 s)		b (200 s)		c (400 s)		d (800 s)	
	Q (C)	j (mA)	Q (C)	j (mA)	Q (C)	j (mA)	Q (C)	j (mA)
Volumetric (per cm^3)	48±3	481±29	72±2	358±7	105±3	261±6	150±3	188±4
Geometric (per cm^2)	11±1	113±7	17±0	85±2	25±1	62±2	35±1	44±1
Gravimetric (per g, total)	17±1	168±10	25±1	125±3	36±1	91±2	52±1	66±1
Gravimetric (per g, active)	50±5	502±47	57±1	282±4	80±2	201±5	115±2	144±3

High performance core-shell Ni/Ni(OH)$_2$ electrospun nanofiber anodes for decoupled water splitting

Supporting Information

S1. Electrode synthesis

S1.1 Electrospun Ni and NiCo substrate synthesis

Precursor solutions were prepared by dissolving 10.6 wt.% nickel acetate tetrahydrate (NiAc, Sigma Aldrich, 98% purity) in a mixture of acetic acid and ethanol (6:4 weight ratio). The solution was stirred overnight at ambient temperature and filtered using a Millex syringe filter unit (0.22 µm pore size) to achieve a light-green clear solution. Next, polyvinyl pyrrolidone (PVP, Mw~1,300,000, Sigma Aldrich) was added to the NiAc solution to a final content of 8.8 w.t% (1.2:1 NiAc:PVP weight ratio) and stirred at ambient temperature until a homogenous viscous solution was achieved. For cobalt-doped electrodes, cobalt acetate tetrahydrate (Sigma Aldrich, ≥98% purity) was added to the precursor solution to a final composition of Ni$_{0.9}$Co$_{0.1}$. The viscosity of the resulting solutions was measured using a viscosity meter (DV-II, BROOKFIELD, Stoughaton, MA, USA), with typical viscosities of ranging between 500-650 cPs.

Figure S1 presents the electrode synthesis process. The solution was electrospun (NS24 multi-nozzle ES machine, Inovenso Ltd.) using a 21-gauge needle at voltage of 17 kV, at a feed rate of 1.25 ml/h and tip-to-collector distance of 15 cm, resulting in "green" electrospun NiAc-PVP fiber mats (Figure S1a). The "green" fiber mats were then calcinated in an air atmosphere (Figure S1b) to form NiO fiber mats (Figure S1c). The resulting NiO mats were gently ground using pestle and mortar to form a coarse powder (Figure S1d) that was then mixed with a 10.5 wt.% binder solution of Poly(propylene carbonate) to form a paste (Figure S1e). The powder-binder composite paste was then pressed at ~3000 kgf to form a pellet having a diameter of ~1.1 cm (Figure S1f). Each pellet was heated in a tubular furnace under reducing atmosphere (5 vol.% H$_2$/N$_2$, 45 cc/min), to decompose the polymer and reduce the NiO to metallic Ni, and to sinter the fibers. SEM images of the green fibers, the calcined fibers, the ground fibers and the final fibers after reduction are presented in Figures S2, S3, S4, and S5, respectively. Qualitative mapping and quantitative elemental analysis were carried out by EDS (Oxford SDD EDS). The mapping is presented in Figure 4 of

the article, and the elemental analysis is summarized for the undoped and doped electrodes in Tables S1 and S2, respectively. The total porosity of the as-prepared Ni substrates was calculated as 74-75%

S1.2 Nickel hydroxide active layer formation

S1.2.1 Layer formation by galvanostatic cycling

Prior to layer formation, each nickel substrate was aged in 5M KOH at 95°C for 2h, to initialize the growth of $Ni(OH)_2$, as shown in Figure S6. In order to grow the active $Ni(OH)_2$ layer from within the nickel fibers, each nickel substrate was connected as the working electrode (WE) to a potentiostat (Ivium-n-Stat multichannel Potentiostat/Galvanostat) in a two-electrode configuration with a nickel foam (15 cm^2) counter electrode (CE) in 5M KOH aqueous electrolyte solution heated to 55±5°C. The electrical connection covered an area of approx. 0.05 cm^2 of the substrate, such that the active area for layer formation was 0.9 cm^2 (geometric cross-sectional area). Each WE was subjected to 60 galvanostatic oxidation-reduction cycles at a current density of ± 200 mA/cm^2 (normalized by the geometric area) to a total charge of ± 150 C/cm^2 or until reaching cutoff potentials of 1.55 V and 1 V_{RHE} during charging and discharging, respectively.

During $Ni(OH)_2$ the process of electrochemical layer growth, the electrode we periodically dried and weighed to estimate the extent of layer growth with cycles (Figure S7a). The substrate was weighed before and after layer growth (m_i and m_f, respectively), and the percent of nickel atoms oxidized to $Ni(OH)_2$ was then calculated from the weight gain (Δm) (eqn. S1):

$$\%Ni \text{ oxidized to } Ni(OH)_2 = \frac{\frac{m_i}{Mw_{Ni}} - \frac{\Delta m}{Mw_{(OH)_2}}}{\frac{m_i}{Mw_{Ni}}} \qquad \text{(S1)}$$

As the active layer builds, the charge capacity of the electrode increases. To estimate the added charge capacity resulting from layer growth progression, the substrate was also subjected to potentiostatic charge-discharge cycles. Figure S7b shows the change in the electrode's charge capacity with layer growth cycles. The most significant change in weight and charge occurred during the first 20 layer-formation cycles. During the 40 additional cycles, a slight increase of only about 5.5 wt.% was observed, while the charge remained approximately unchanged, implying that there is a critical thickness above which ions (OH$^-$) cannot penetrate the layer. Furthermore, the increased charge capacity is only observed for long charge-discharge tests of over 800 s. This could be attributed to a diffusion limitation, with OH$^-$ ions requiring a relatively long time to diffuse into the thick layer. By the end of the process, the electrode's weight was

increased by 18% relative to the initial substrate weight, corresponding to a conversion of 30% of the Ni atoms to $Ni(OH)_2$. The SEM images for the undoped NFA before and after layer formation are presented in Figure 3 of the article. The structure of the cobalt-doped NFA was similar to that of the undoped NFA, as shown in Figures S8.

S1.2.2 Layer formation by E-TAC cycling and cycling stability test

An as-prepared Ni NF substrate was connected as the WE in a three-electrode configuration with a Pt foil (6 cm^2) CE and an Hg/HgO/1M NaOH RE in 5M KOH aqueous electrolyte at ambient temperature. During the charging step, the WE was subjected to a constant potential polarization at 1.48 V_{RHE} for 100s. After 100 s, the WE was disconnected and dipped in a hot (95°C) 5M KOH solution for 100s. This cycle was repeated 100 times. The same test was repeated for a cobalt-doped EDA, and the results are presented in Figure S9. X-ray diffractograms and SEM images of the resulting $Ni(OH)_2$ layer on the NFA are presented in Figures S10 and S11, respectively. For both the NFA and the EDA, an initial drop in charge density was observed, followed by a stabilization at approximately 20 and 10 C/cm^3, respectively. The initial drop may be attributed to the change in SOC, as the anode is completely discharged prior to the test, and its SOC gradually increases until stabilization is reached. In this test, the active $Ni(OH)_2$ layer was grown onto the porous nickel substrate in situ by E-TAC cycling, which could explain the longer cycling required to reach stabilization for this anode.

S2. Electrodeposited anodes

The EDAs were prepared by electrochemical deposition of $Ni(OH)_2$ onto a conductive nickel foam (Ni-4753, RECEMAT, 95.2% porosity with 400 μm average pore size), as discussed in Section 2.2 of the article. A digital image of the EDA is presented in Figure S12a. Figures S12b, S12c and S12d show SEM images of the as-received nickel foam, the foam after deposition and of the resulting $Ni(OH)_2$ layer, respectively.

S2.2 Nickel foam surface area measurement

The surface area of the nickel foam substrate for electrochemical deposition was supplied by the vendor[1] and confirmed by electrochemical surface area (ECSA) analysis as 0.01 m^2/g (Figure S13). ECSA (electrochemically active surface area) is evaluated from the electrochemical double-layer capacitance (C_{DL}) of the catalytic surface. C_{DL} is determined by measuring the non-faradaic capacitive current associated with double-layer charging, i_c, from the scan-rate (v) dependence of cyclic voltammograms

(CVs). A plot of i_c as a function of v yields a straight line with a slope equal to C_{DL} . In order to evaluate the ECSA, C_{DL} is divided by the capacitance of an atomically smooth planar surface of the material per unit area (C_s). For a nickel substrate dipped in 1M NaOH electrolyte solution, C_s is estimated to be 25 $\mu F/cm^2$.[2] ECSA tests were carried out in a three-electrode configuration in 1M NaOH at ambient temperature, with the nickel substrate (nickel foam, or electrospun substrate) connected as the working electrodes with an Hg/HgO/1M NaOH reference electrode and a platinum foil (6 cm^2) counter electrode.

S3. Electrochemical tests

S3.1 ETAC tests

Each electrode was subjected to charge-regeneration (E-TAC) cycles, as described in Section 2.5 of the article. For tests carried out potentiostatically (at 1.48 V_{RHE} or 1.43 V_{RHE}), the current was recorded, and the charge was calculated by integrating the current over time. Typical current responses for each electrode (after stabilization was reached) for test durations (charging duration = regeneration duration) of 100, 200, 400 and 800 s are presented in Figure S14 and S15 for charging potentials of 1.48 V_{RHE} and 1.43 V_{RHE}, respectively. The results are summarized in Figure 7 of the article.

The same tests were repeated for each anode with the charging durations varied between 100 s and 800s, while maintaining the regeneration duration at 100 s. The charge that could be extracted with only 100 s ($Q_{regen, 100s}$) was then compared to the charge that was extracted with equal charging and regeneration durations ($Q_{regen, equal}$). Figure S16 shows the ratio $Q_{regen, 100s}$ / $Q_{regen, equal}$ for the undoped NFA, cobalt-doped NFA and EDA.

To compare the performance of the NFAs to our previously reported EDA,[3] an E-TAC test was carried out at a constant current density using a champion cobalt-doped NFA. The cobalt-doped NFA was connected as a WE with a Pt-coated Ti mesh cathode (1 cm^2) in 5M KOH aqueous electrolyte. The hydrogen generation steps were carried out at ambient temperature at a constant current density of 50 mA/cm^2 (normalized by the geometric area) for 100 s, followed by oxygen generation steps at 95°C in 5M KOH for 100 s, similarly to the conditions in our previous report.[3] Figure S17 shows the results obtained with the cobalt-doped NFA overlaid on the results reported in Figure 3a of ref.[3] for a cobalt-doped EDA. The active layer in both the NFA and EDA had a similar composition ($Ni_{0.9}Co_{0.1}(OH)_2$). Although the hydrogen evolution overpotential at the cathode (inset in Figure S17) was slightly higher in

this test (115 mV, compared to 80 mV in the previous report),[3] the low charging potential of the cobalt-doped NFA (1.36 V_{RHE} on average throughout the test) compared to the cobalt-doped EDA in our previous report (1.42 V_{RHE}) resulted in an overall lower cell voltage, with an increase in the average voltage efficiency from 98.7%$_{HHV}$ to 100%$_{HHV}$ using the NFA.

S3.2 Electrochemical charge-discharge tests

S3.2.1 The chemically regenerated charge compared to the electrochemical charge

In E-TAC cycling, the charged NiOOH anode is chemically discharged (regenerated) upon contact with a heated (95°C) alkaline solution, as described in the article. Without the application of an electrical bias, the rate of this process is controlled solely by mass transport, i.e., the solid-state diffusion of reactants and products in and out of the NiOOH layer. In addition, the driving force for the regeneration reaction, which corresponds to the electrochemical potential difference between the anode's rest potential and the OER potential ($E_{anode}^{0} - E_{OER}^{0}$), is reduced as the electrode discharges from NiOOH to Ni(OH)$_2$. Therefore, the rate and extent of the chemical regeneration reaction are lower compared to those achieved by electrochemical discharging. To demonstrate this, the anodes were subjected to electrochemical charge-discharge cycles. Each NFA was connected as the WE in a 3-electrode configuration with a Pt CE and an Hg/HgO/1M NaOH RE in 5 M KOH at ambient temperature. The anode was subjected to repeated charge discharge cycles, with charging at 1.48 V_{RHE} for a set duration of 100, 200, 400 or 800 s (similarly to the E-TAC tests) and discharging at 1.23 V_{RHE} for the same duration. A discharging potential of 1.23 V_{RHE} was chosen since this is the standard OER potential, and therefore it is the lowest potential that the NiOOH anode can reach upon chemical regeneration. Figure S18 presents the ratio between the chemically regenerated charge ($Q_{regen} = Q_{regen, \, equal}$) and the electrochemically discharged charge (Q_{dis}) for each charging duration (which is equal to the regeneration duration in the E-TAC tests and to the discharging duration in the electrochemical tests). For shorter tests, the ratio between Q_{regen} and Q_{dis} is the highest, and it decreases with test duration. This is consistent with the regeneration mechanism, which is mass-transport limited. It can be seen that there is a correlation between Q_{dis} and Q_{regen} for each test duration with $Q_{dis,800s} \approx 0.6 \cdot Q_{regen,800s}$, $Q_{dis,400s} \approx 0.5 \cdot Q_{regen,400s}$, $Q_{dis,200s} \approx 0.4 \cdot Q_{regen,400s}$, and $Q_{dis,100s} \approx 0.35 \cdot Q_{regen,100s}$.

S3.2.2 Preliminary electrochemical characterization of NFAs with different morphologies

NFAs with various morphologies were achieved by modifying the electrospinning and thermal treatment parameters, as discussed in Section 2.4 of the article. Several sintering temperatures were tested (500, 600, and 700°C), with 2h at each temperature, while all other process parameters were unchanged. The SEM images of the resulting NFAs are presented in Figures 8a-c of the article. The calculated porosity was ~75% for all three NFAs, with a density of ~2.23 g/cm^2 and a thickness of ~0.24 mm. To compare their performance, the electrodes were ages in 5M KOH for 2h at 95°C to initiate the growth of $Ni(OH)_2$, and then subjected to electrochemical charge-discharge cycles (see Section S3.2.1). The results are shown in Figure S19a, normalized by the anodes' volume. Next, the effect of fiber diameter was examined. Thinning the fiber diameter was achieved by diluting the precursor solution, resulting in a twofold decrease in viscosity (from ~600 cPs to ~300 cPs). Moreover, the applied voltage during electrospinning was raised from 14 kVs to 26 kVs. The SEM image of the resulting fibers is shown in Figure 8d of the article, and the electrochemical shown in Figure S19b. Based on the results presented in Figure S18, the volumetric charge capacity of the thin-fiber NFA is projected to reach ~164 C/cm^3, which is roughly 30% greater than its thick-fiber (undoped) counterpart, and roughly 10% greater than the thick-fiber cobalt-doped NFA.

S3.3 Steady state oxygen evolution current tests

In order to measure the steady-state oxygen evolution reaction (OER) current, each nanofiber anode was connected as the working electrode (WE) to a potentiostat (Ivium-n-Stat multichannel Potentiostat/Galvanostat) in a two-electrode configuration with a Pt (1 cm^2) counter electrode (CE) in 5M KOH aqueous electrolyte solution at ambient temperature. Each WE was then charged potentiostatically at 1.43, 1.44, 1.46, 1.48 and 1.5 V_{RHE} for 60 minutes. This duration was enough to reach stabilization of the current (Figure S20).

S4. Dissolved oxygen tests

Dissolved oxygen (DO) tests were carried out in a three-electrode system, with a cobalt-doped NFA as the working electrode and an Hg/HgO/1M NaOH as the reference electrode. The counter electrode was a 5 cm^2 electrodeposited $Ni(OH)_2$ electrode that was charged to NiOOH prior to operation. During operation, the counter electrode was discharged from NiOOH to $Ni(OH)_2$ to avoid hydrogen evolution in the cell. The test cell was filled with an aqueous solution of 5M KOH at ambient temperature, with the DO sensor (Hamilton VisiFerm mA) dipped in the solution. The cell was sealed and purged with nitrogen (N_2) gas for 30 min prior to each measurement. Measurements were carried out under a slight nitrogen

overpressure (~20 mbar) while stirring. For each test duration/potential, several E-TAC cycles were carried out outside of the measurement cell until stabilization of the current response was achieved. Then, the anode was regenerated again and placed in the measurement cell, wherein the same potential was applied (either 1.48 V$_{RHE}$ or 1.43 V$_{RHE}$) to the same charge as in the previous E-TAC cycles. The resulting Faradaic efficiency for various charging/regeneration durations (100, 200, 400 and 800 s) are presented in Figures S21a and S21b for charging potentials of 1.48 and 1.43 V$_{RHE}$, respectively.

S4.1 Faradaic efficiency approximation from electrochemical tests

At each charging potential, the maximal rate of oxygen evolution is the steady-state OER rate, as discussed in Section S3.3. However, it can be assumed that the OER proceeds at a lower rate during initial charging of the Ni(OH)$_2$ anode and increases in rate as the anode's state of charge (SOC) increases. Accordingly, the *lower limit* of the Faradaic efficiency of the Ni(OH)$_2$ charging reaction at a given applied potential can be calculated from the steady-state OER rate at the same potential:

$$\eta_{F,L} = 1 - \frac{Q_{OER,max}}{Q_{total}} = 1 - \frac{i_{OER,max} \cdot t}{<i_{total}> \cdot t} = 1 - \frac{i_{OER,max}}{<i_{total}>} \text{ , eqn. S1}$$

Where $\eta_{F,L}$ is the lower limit Faradaic efficiency, $Q_{OER,max}$ is the maximum OER charge, Q_{total} is the total charge, $i_{OER,max}$ is the maximum OER current, $< i_{total} >$ is the average total current, and t is the charging duration.

Figure S22 presents the calculated $\eta_{F,L}$ for the charging of a cobalt-doped NFA during the E-TAC tests presented in Figure 7 of the article, and its comparison to the measured Faradaic efficiency from dissolved oxygen measurements, which are presented in Figure S21. It can be seen that, within the error margins, the calculated $\eta_{F,L}$ does not surpass the measured η_F. Thus, the steay-state OER test can be used as a preliminary Faradaic efficiency tool that does not require DO measurement.
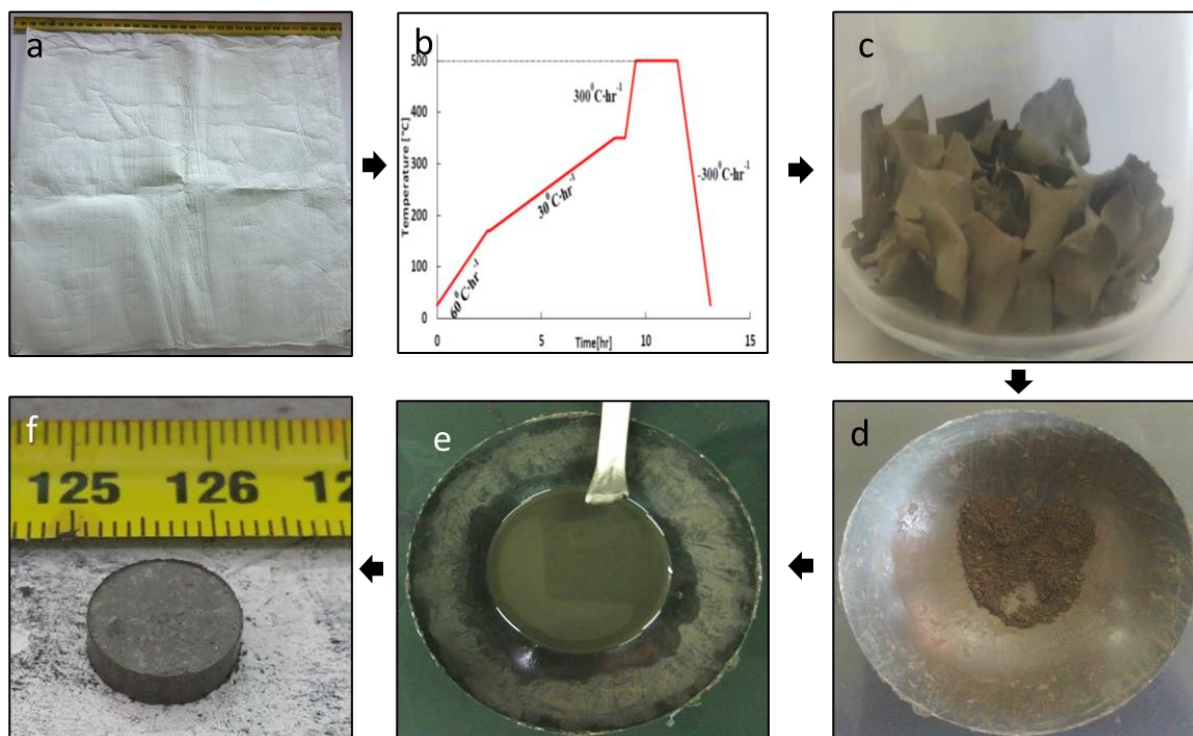
Figure S1: Electrode synthesis process. (a) Electrospun NiAc-PVP "green" fiber sheet; (b) Thermal profile of the calcination step; (c) NiO fiber mats after calcination; (d) NiO nanofiber coarse powder; (e) NiO nanofiber powder and PPC paste; and (f) Metallic nickel porous substrate..
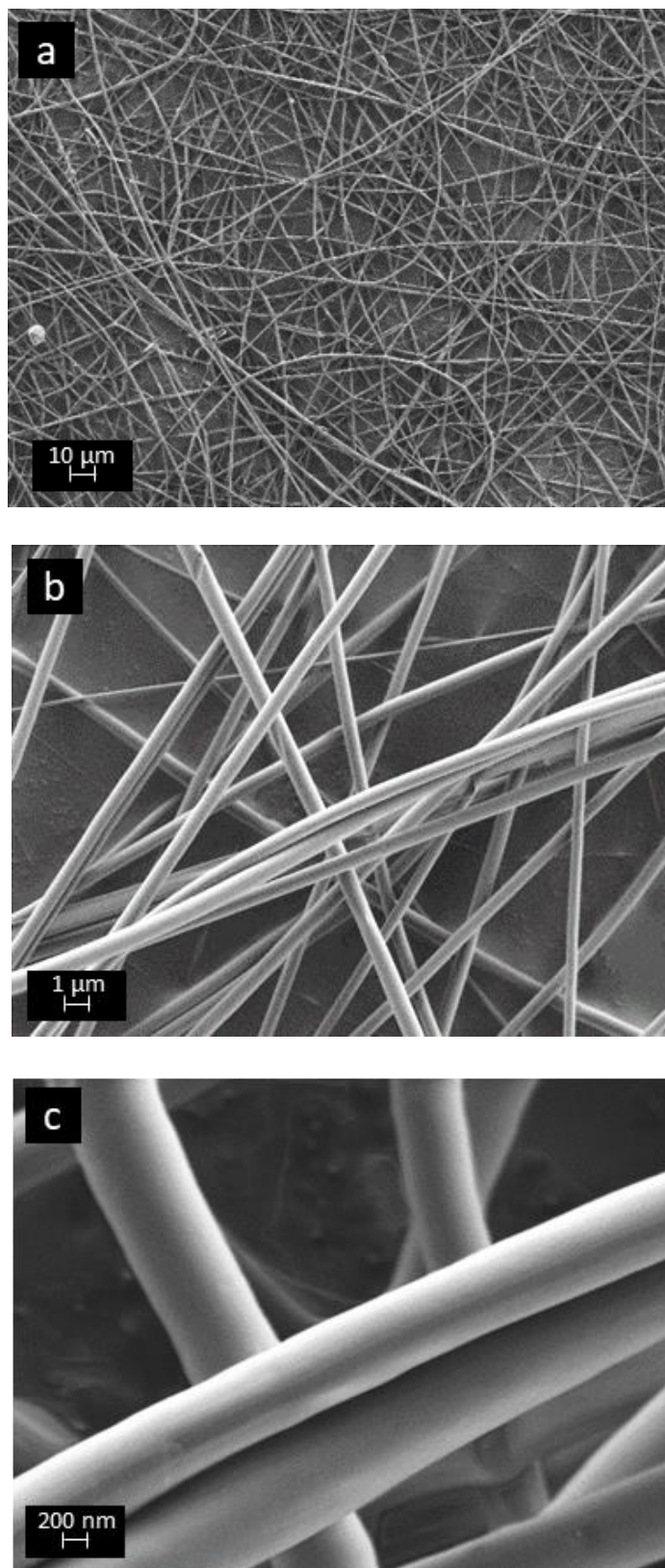
Figure S2: HRSEM micrographs of NiAc-PVP "green" nanofibers under various magnifications. (a) x1,000, (b) x10,000, and (c) x50,000.
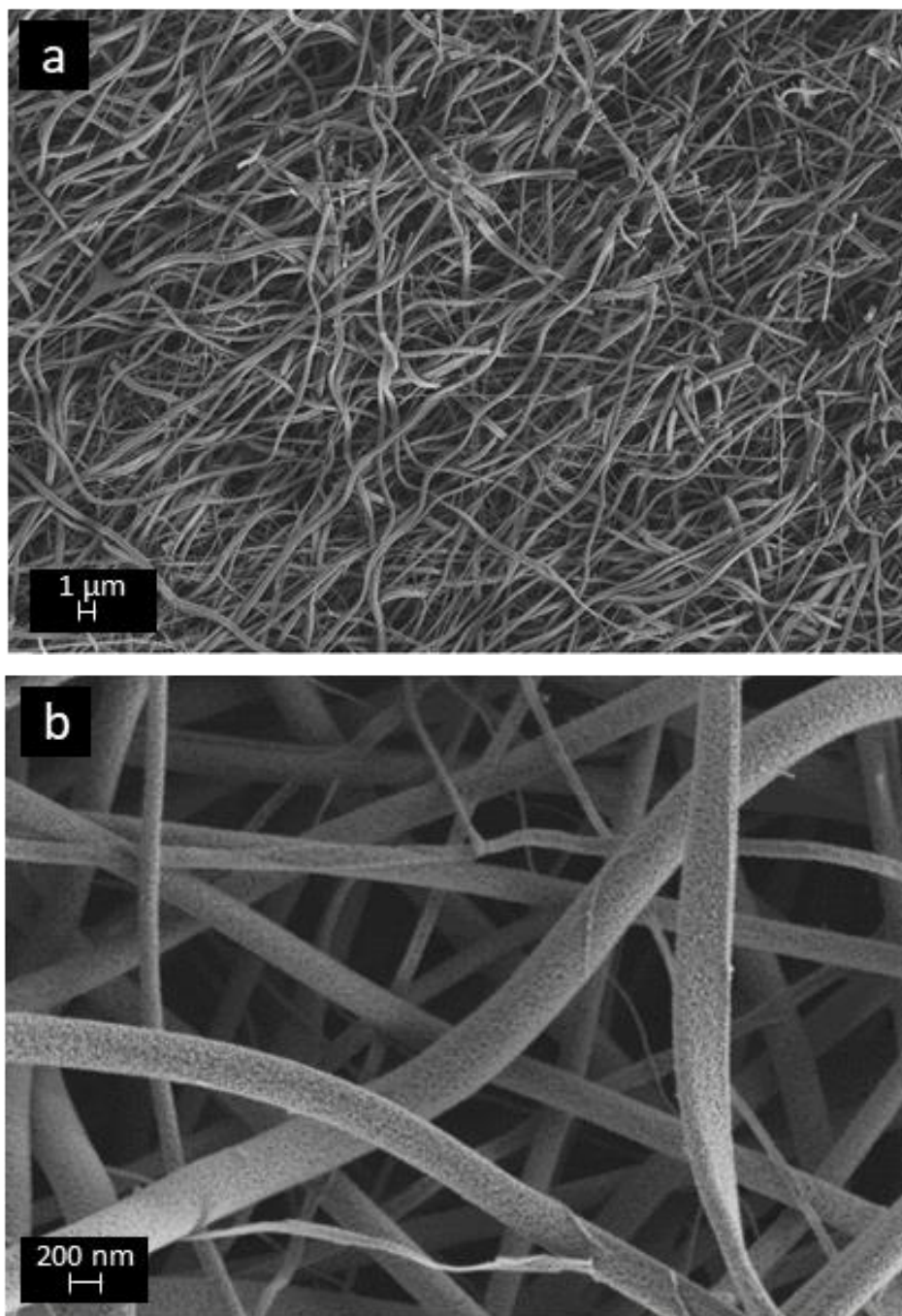
Figure S3: HRSEM micrographs of nickel oxide nanofibers after calcinations. (a) low-, and (b) high-magnification.
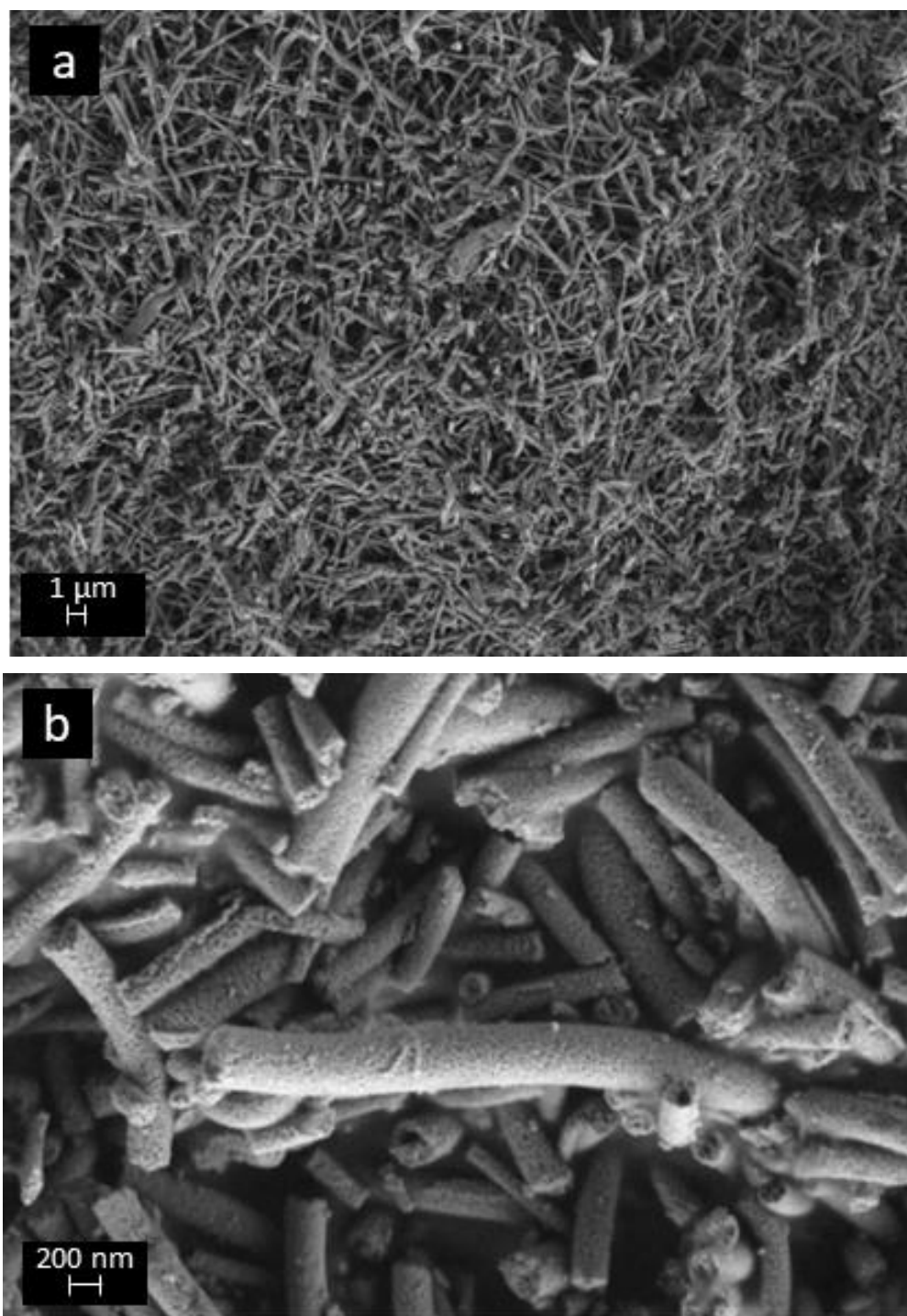
Figure S4: HRSEM micrographs of nickel oxide nanofibers after grinding and binder addition. (a) low-, and (b)high-magnification.
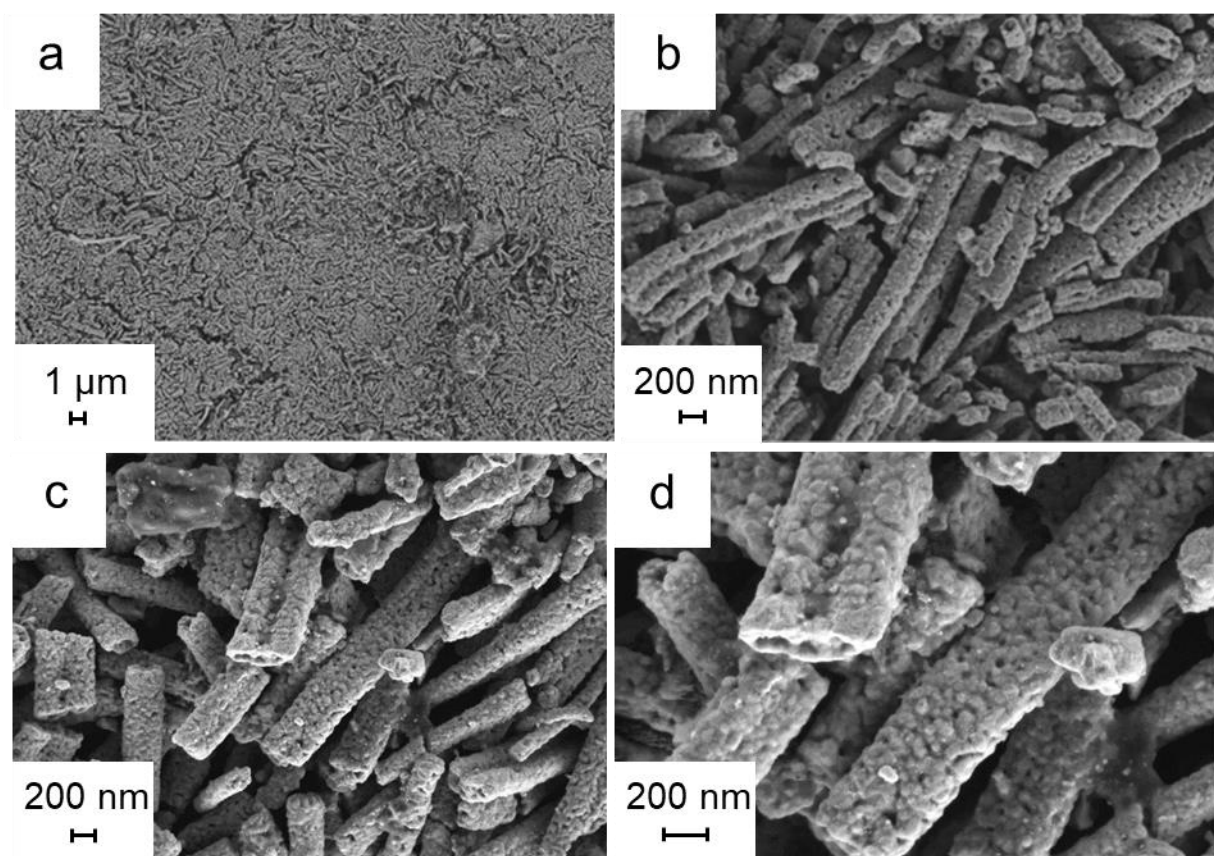
Figure S5: HRSEM micrographs of a pressed and reduced nickel substrate at various magnifications.
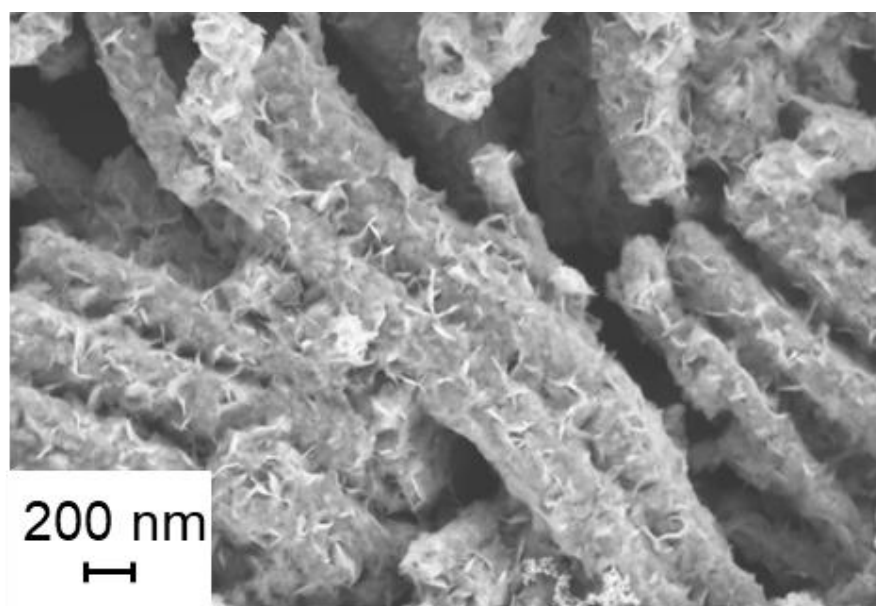
Figure S6: HRSEM micrographs of the reduced nickel substrate after aging for 2h in 5M KOH at 95°C.
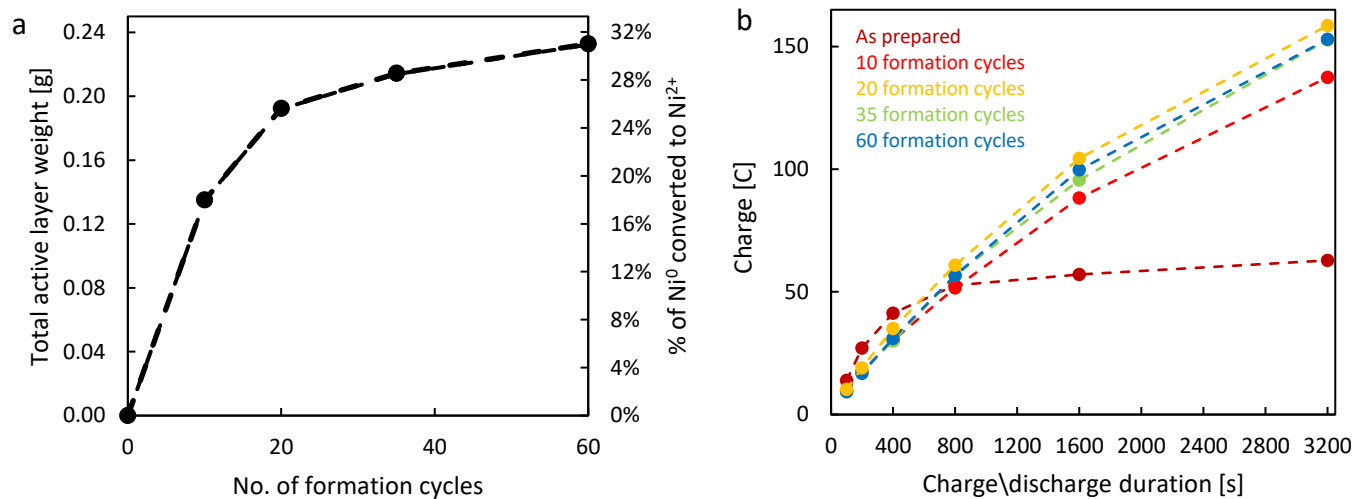
Figure S7: Ni(OH)$_2$ layer growth (a) and the corresponding change in electrode charge capacity (b) with layer formation cycles. The charge capacity was estimated using potentiostatic charge/discharge cycles at 1.48 V$_{RHE}$/1.23 V$_{RHE}$ for charging/discharging durations of 100, 200, 400, 800, 1600, and 3200 s in 5M KOH electrolyte at ambient temperature.
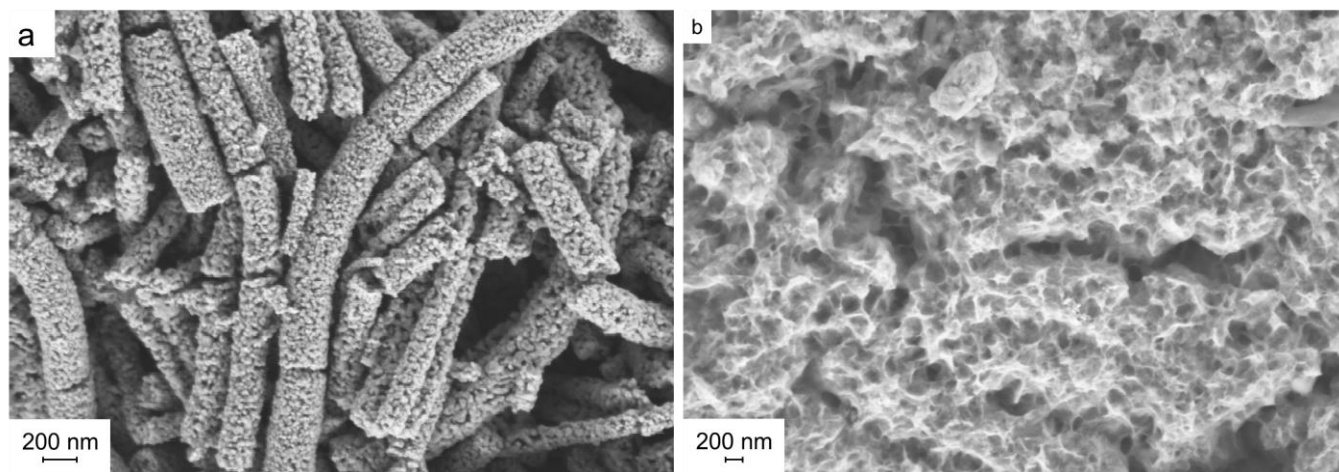
Figure S8: HRSEM images of a cobalt-doped Ni/Ni(OH)$_2$ nanofiber anode. (a) As-prepared cobalt-doped Ni nanofiber substrate. (b) Ni/NiCo(OH)$_2$ nanofiber anode after E-TAC water splitting tests.
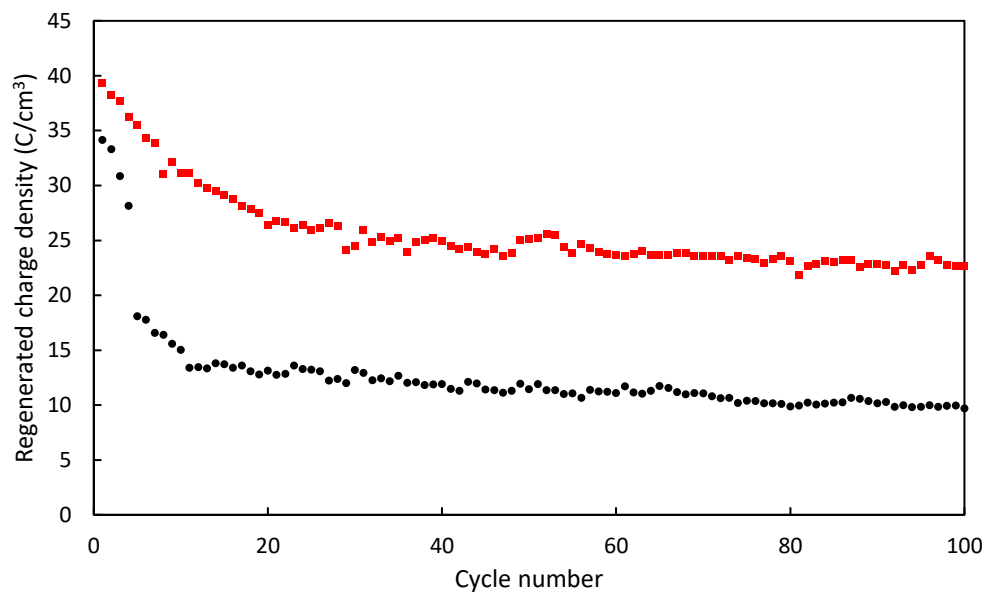
Figure S9: Cycling stability test. The regenerated charge as a function of cycle number throughout 100 E-TAC water splitting cycles with an undoped Ni/Ni(OH)$_2$ NFA (red datapoints) and EDA (black datapoints). Charging was carried out by applying a constant potential of 1.48 VRHE in 5M KOH at ambient temperature for 100 s, and regeneration was carried out by dipping the charged anode in 5M KOH at 95°C for the same duration.
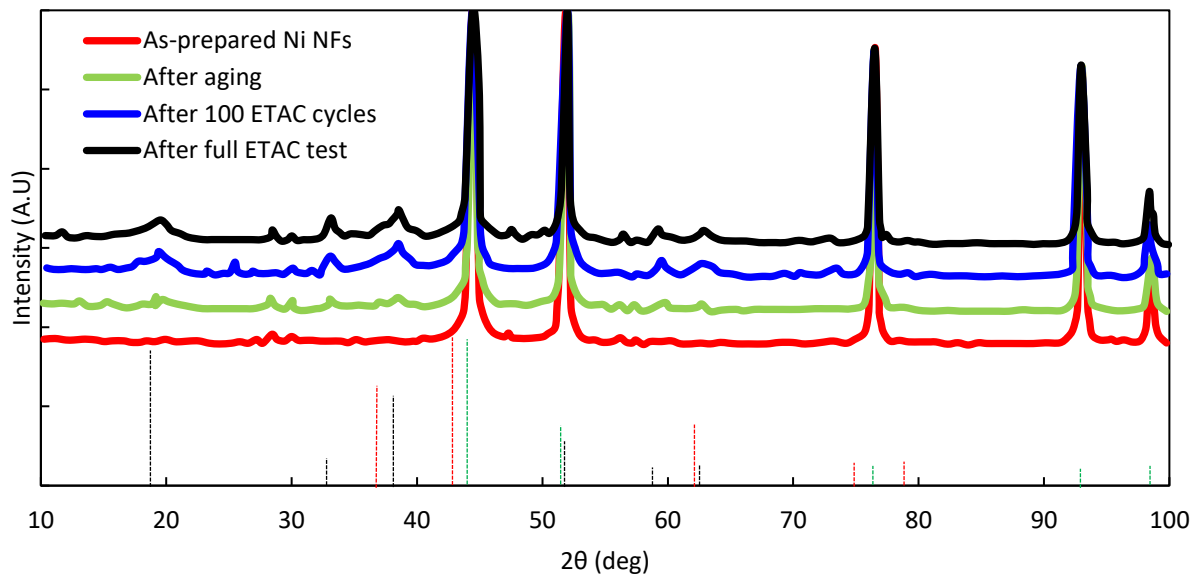
Figure S10: X-ray diffractograms of an undoped Ni/Ni(OH)$_2$ NFA formed by E-TAC cycles after different preparation stages: as-prepared NF nickel substrate (red line), after aging for 2 h in 5M KOH at 90°C (green line), after 100 E-TAC cycles of 100s charge / 100s regeneration (blue line), and after final characterization in a full E-TAC test (black line). The dashed vertical lines indicate the position and relative intensities of Bragg reflections of metallic nickel (JCPDS 00-004-0850, green), NiO (JCPDS 01-071-4750, red) and β-Ni(OH)$_2$ (JCPDS 00-059-0462, black).
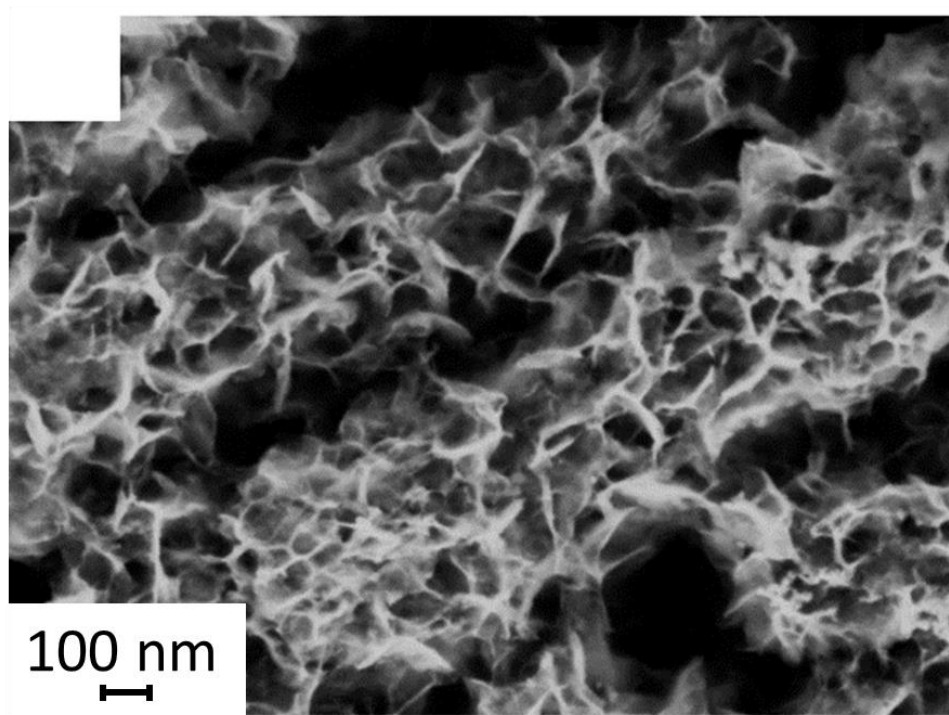
Figure S11: HRSEM image of an undoped Ni/Ni(OH)$_2$ NFA after layer growth by E-TAC cycling. (b)
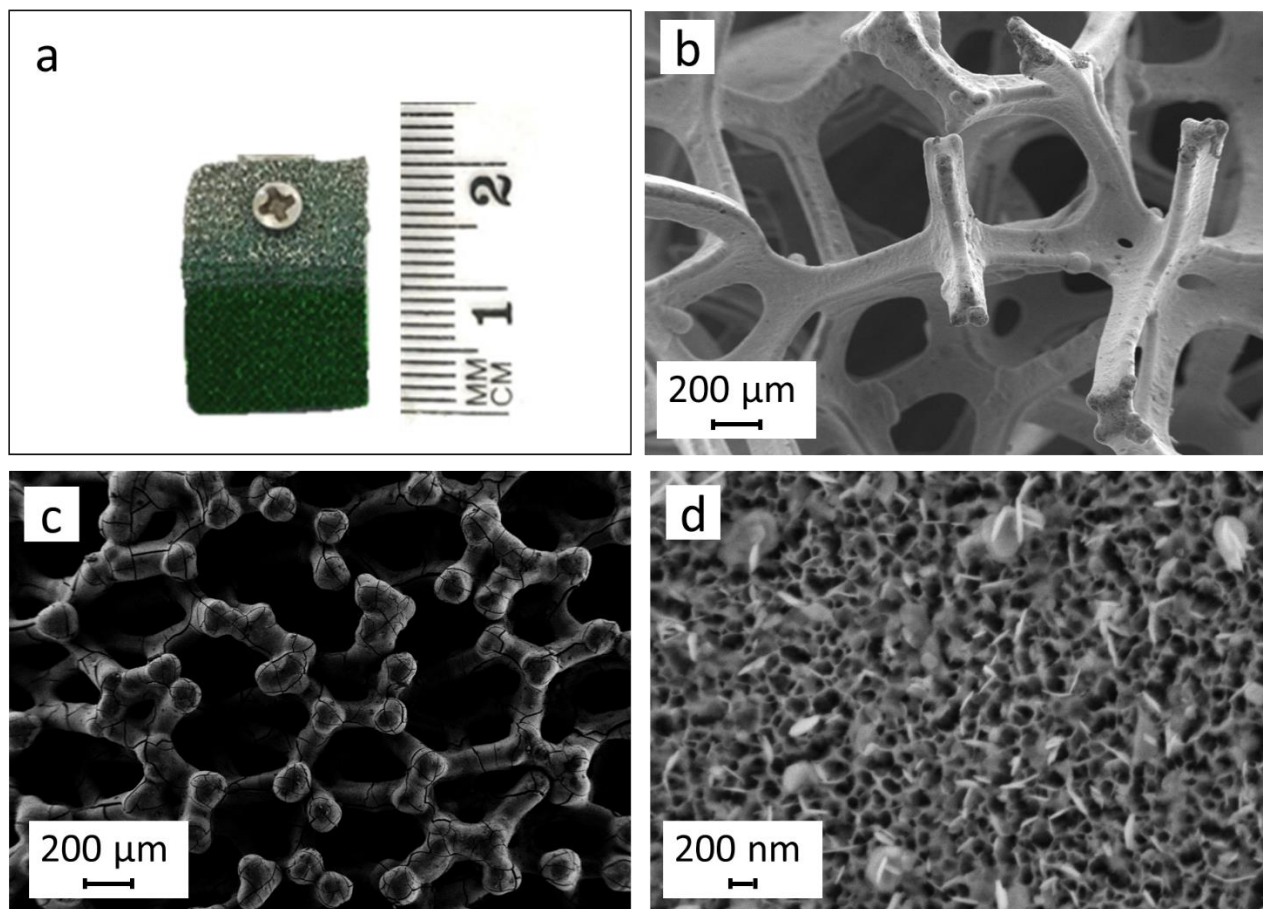
Figure S12: (a) digital image of an EDA deposited onto nickel foam. (b)-(d) HRSEM images of the as-received nickel foam (b), the EDA after deposition (c), and the resulting $Ni(OH)_2$ layer (d).
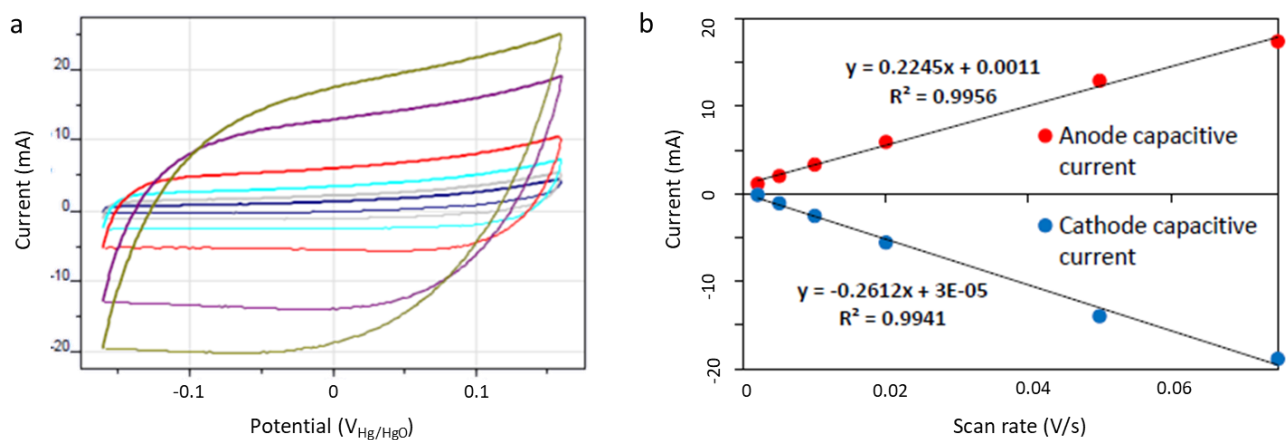
Figure S13: Electrochemically active surface area tests. (a) Cyclic voltammograms of a nickel foam electrode in 5M KOH aqueous electrolyte at scan rates of 0.02 – 0.075 V/s. (b) Anodic and cathodic currents at 0 $V_{Hg/HgO}$ as a function of the scan rate.
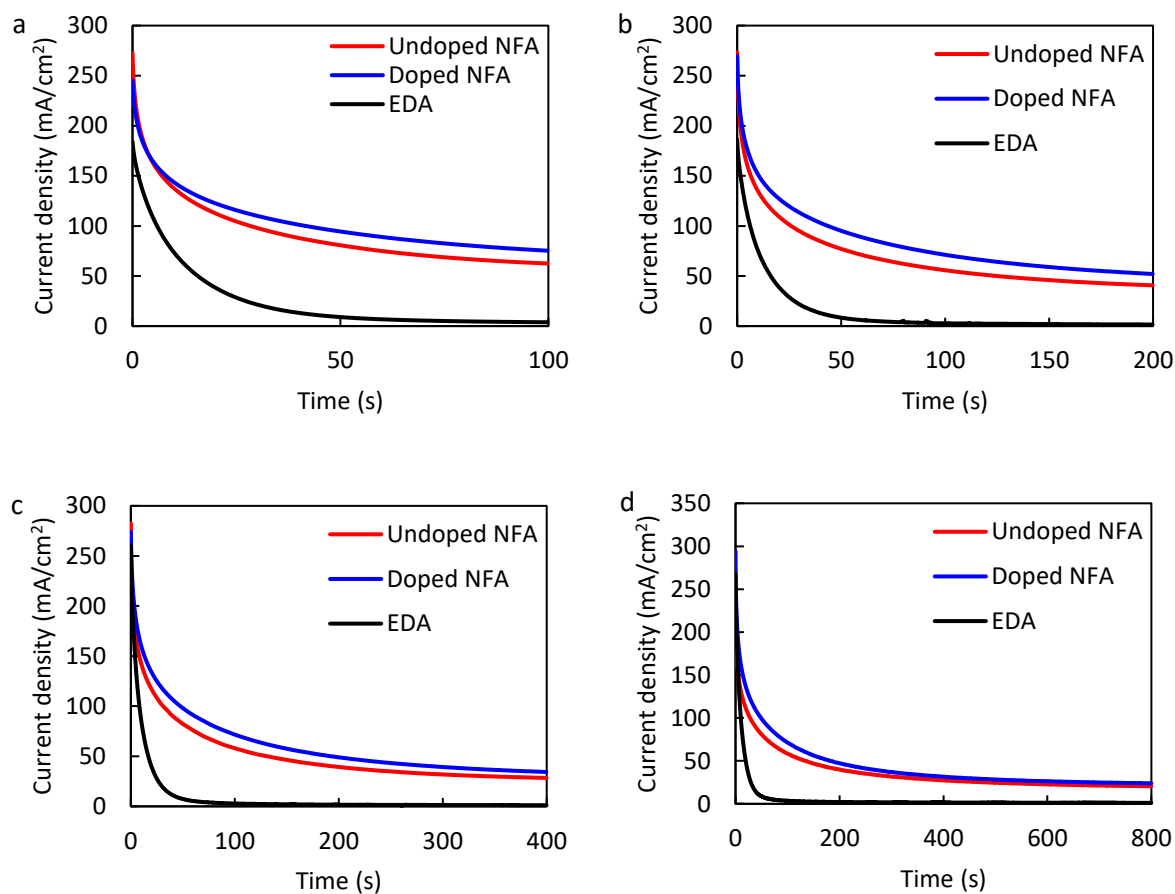
Figure S14: Potentiostatic current traces at 1.48 V_{RHE} for an undoped NFA (red), a cobalt-doped NFA (blue) and an EDA (black) during the charging step of E-TAC cycles carried out at equal charge-discharge durations of 100s (a), 200 s (b), 400 s (c), and 800 s (d).
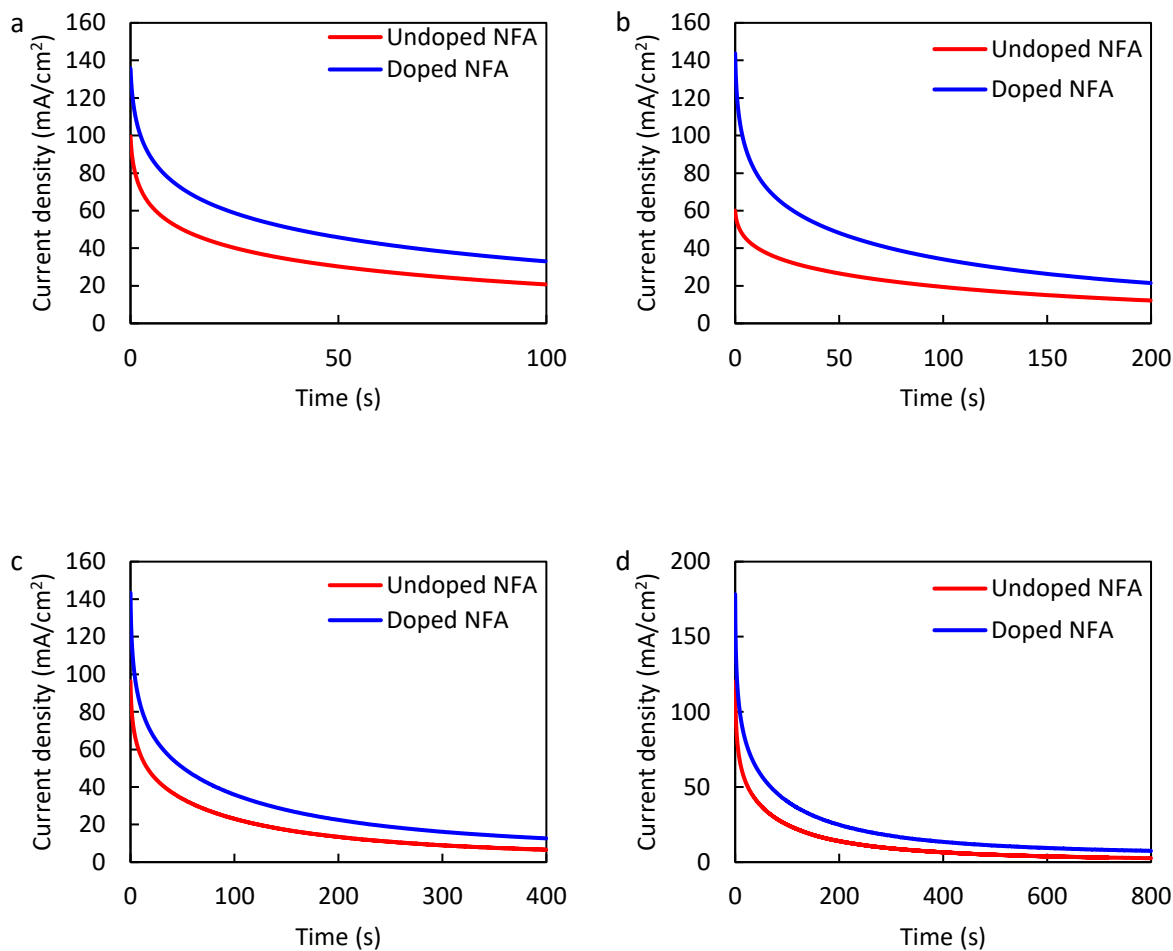
Figure S15: Potentiostatic current traces at 1.43 V_RHE for an undoped NFA (red), and a cobalt-doped NFA (blue) during the charging step of E-TAC cycles carried out at equal charge-discharge durations of 100s (a), 200 s (b), 400 s (c), and 800 s (d).
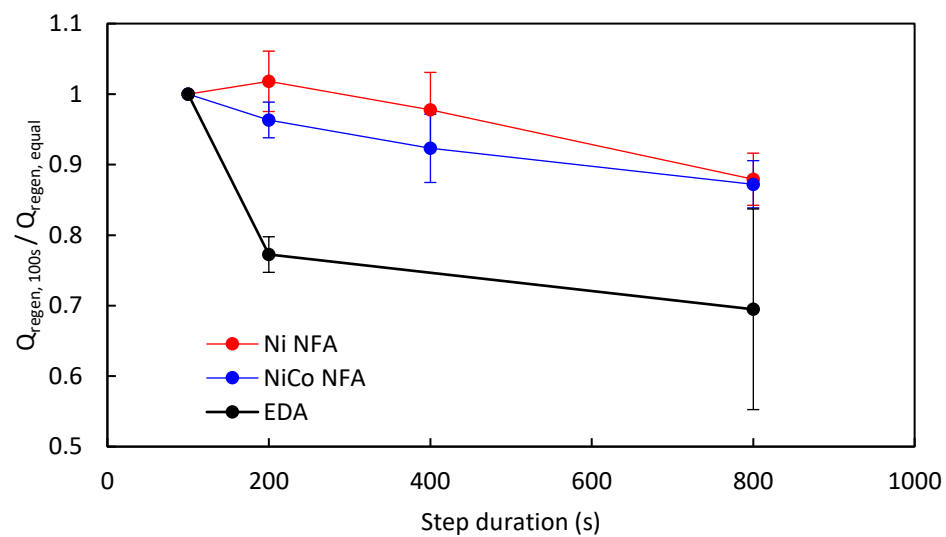
Figure S16: The ratio between the regenerated charge at short (100 s) regeneration duration ($Q_{regen, 100s}$) and the regenerated charge at regeneration step duration equal to the charging step duration ($Q_{regen,equal}$) for undoped (red) and cobalt-doped (blue) NFAs and a cobalt-doped EDA (black).
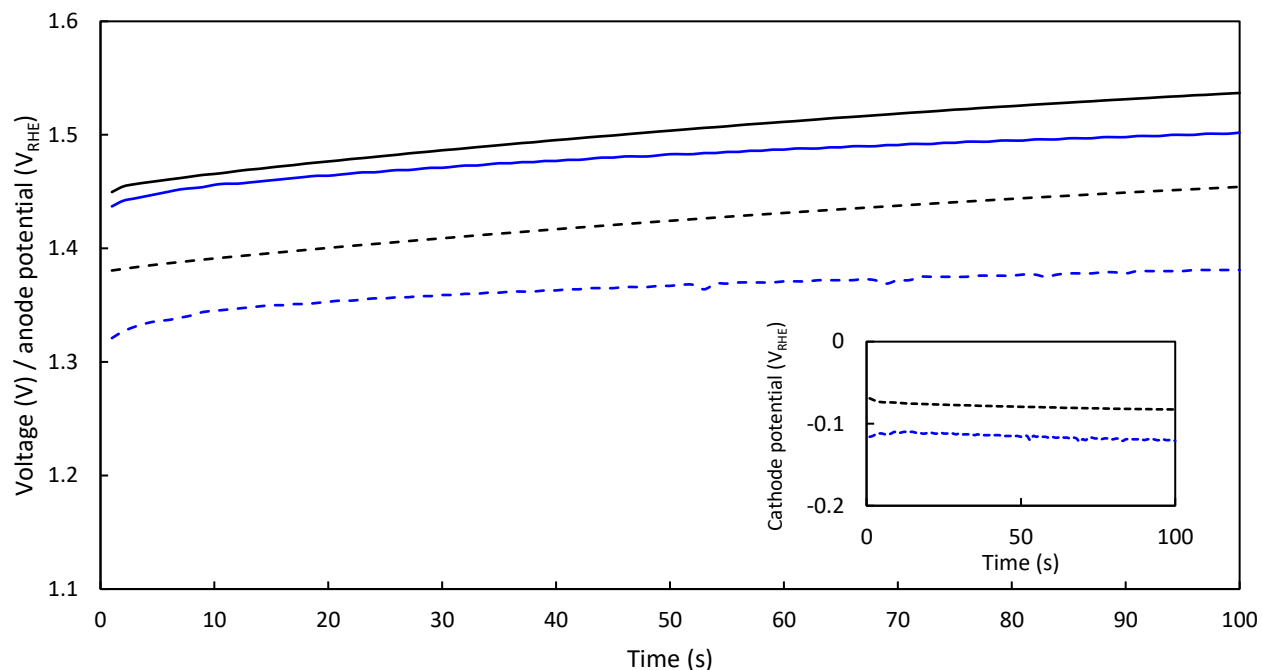
Figure S17: Applied voltage and anode potential during the hydrogen generation step of an E-TAC water splitting test at 50 mA/cm^2. The average anode potentials (dashed line) and corresponding cell voltage (solid line) throughout 6 E-TAC water splitting cycles carried out in this work with a cobalt-doped NFA (blue lines), overlaid with the results obtained, under similar conditions, in our previous report using a cobalt-doped EDA of similar composition (black lines). In both tests, charging was carried out at a constant current density of 50 mA/cm^2 (normalized by the geometric area) in 5M KOH aqueous electrolyte at ambient temperature for 100s, and regeneration was carried out by dipping the charged anode in 5M KOH aqueous electrolyte at 95°C for 100 s. The inset shows the average cathode potential using a platinized titanium mesh in this work, and a platinized nickel-coated SS mesh in the previous report.[3]
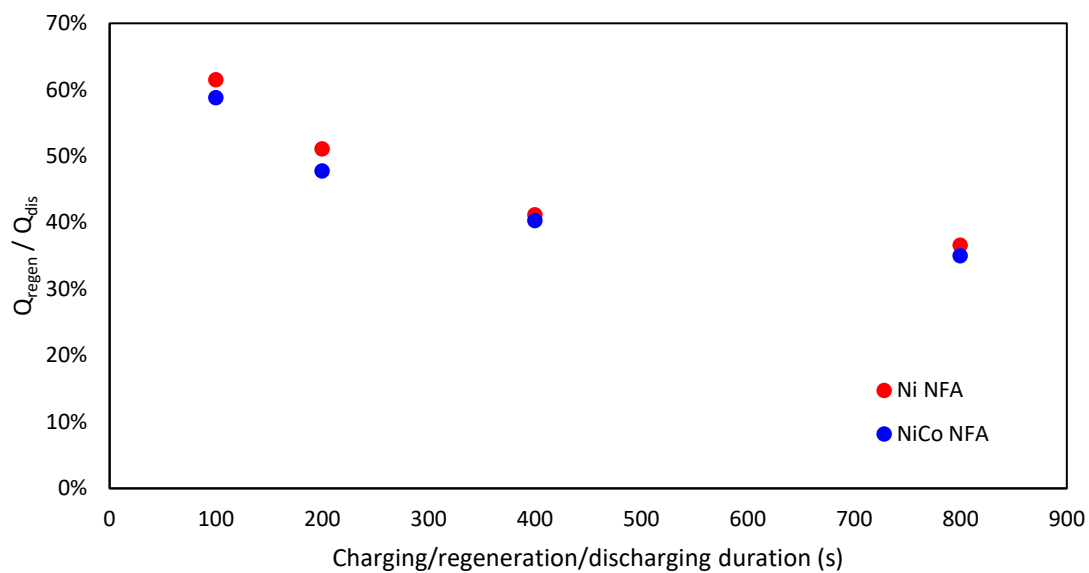
Figure S18: The ratio between the charge that can be regenerated by chemical regeneration in a hot alkaline solution (Q_{regen}) and the charge that can be extracted by electrochemical discharge at a constant potential of 1.23 V_{RHE} (Q_{dis}). Results are shown for an undoped (red) and a cobalt-doped (blue) nanofiber anodes.
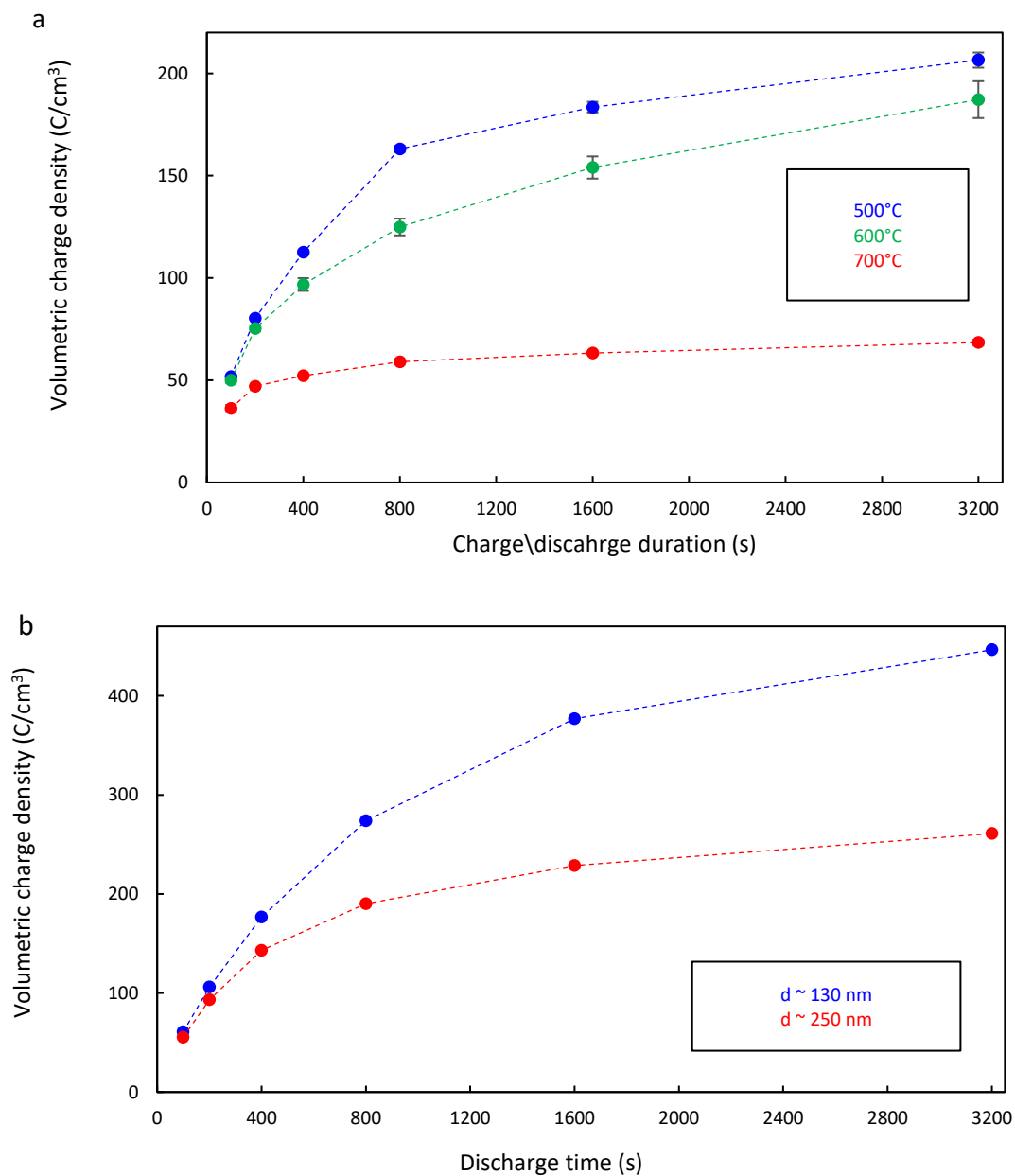
Figure S19: The volumetric charge density obtained by charge-discharge tests for (a) NFAs sintered at 500°C (blue), 600°C (green) and 700°C (red); and (b) NFAs produced from precursor solutions with a high viscosity and low voltage (600 cPs, 14 kVs) resulting in thick nanofibers (red) with a low viscosity and high voltage (300 cPs, 24 kVs) resulting in thin nanofibers (blue).
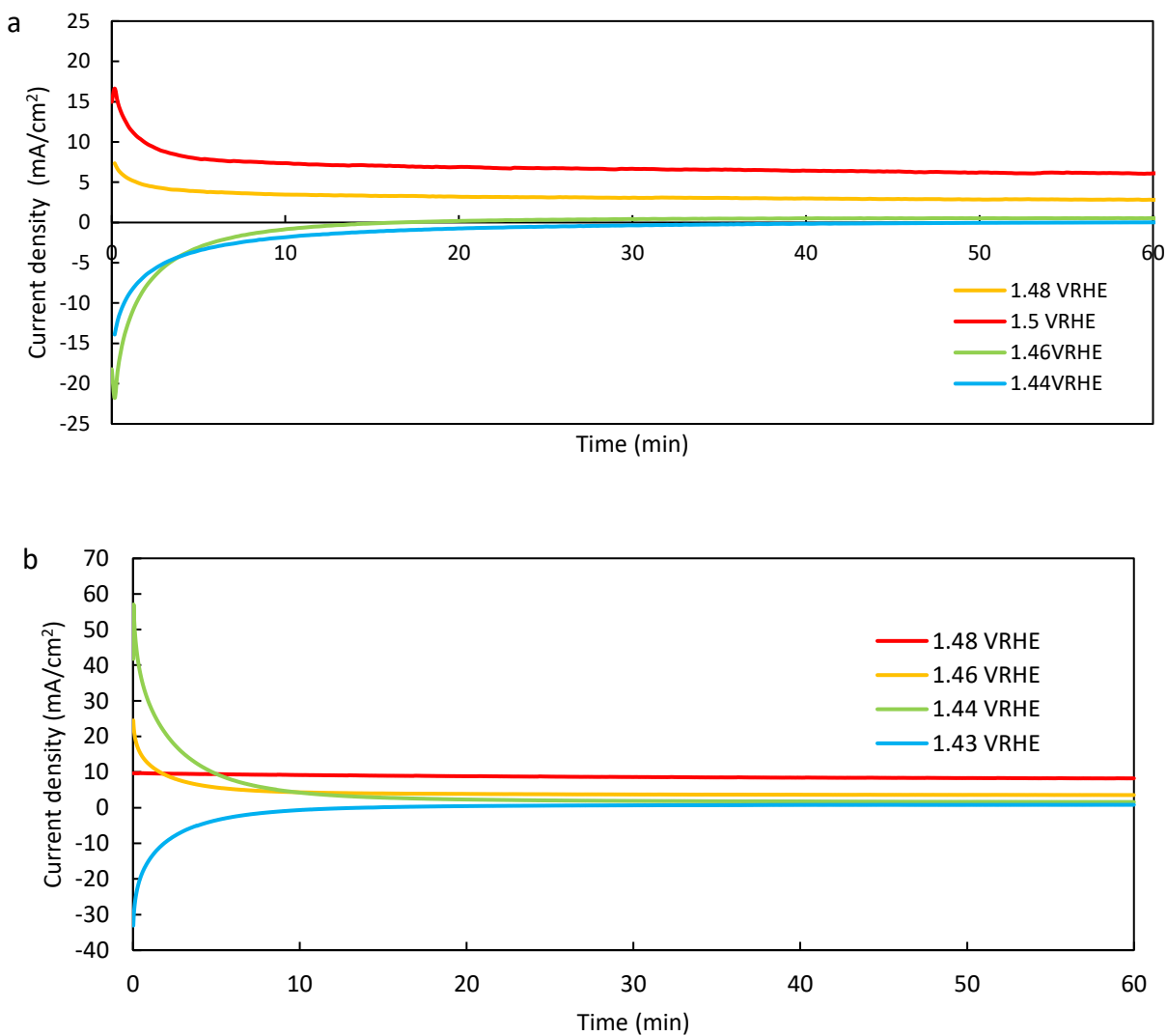
Figure S20: Potentiostatic current traces for undoped (a) and cobalt-doped (b) nanofiber anodes. Each polarization was carried out at a constant potential for 60 min in 5M KOH at ambient temperature.
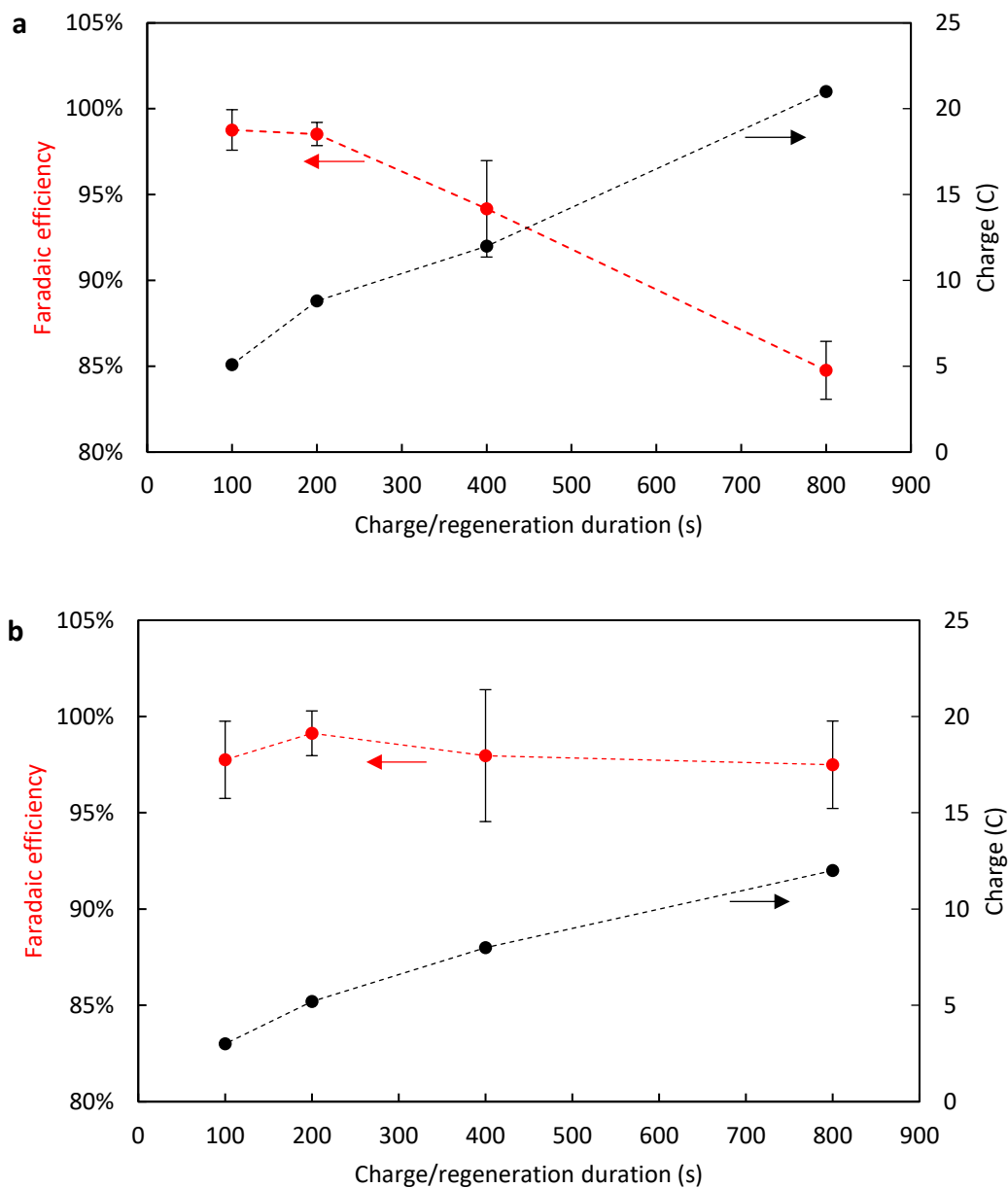
Figure S21: Faradaic efficiency of cobalt doped NFA charging. Comparison of the average Faradaic efficiency of the cobalt doped NFA's charging reaction during E-TAC water splitting tests carried out at 1.48 V_{RHE} (a) and 1.43 V_{RHE} (b) charging potentials. The secondary y-axis displays the total charge that was passed in each E-TAC water splitting cycle.

a

b
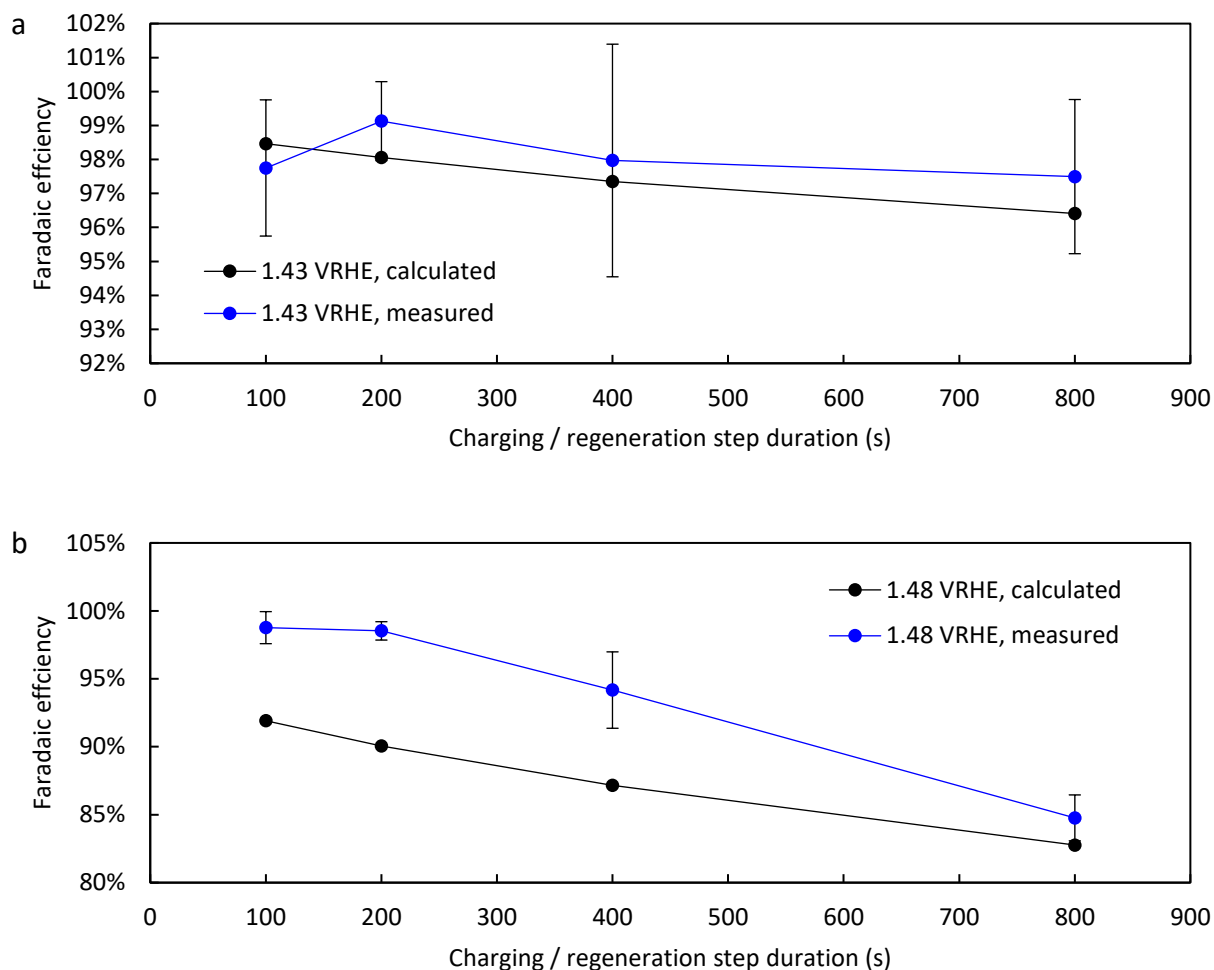
Figure S22: The calculated (black) and measured (blue) Faradaic efficiency of the charging reaction of a cobalt-doped NFA during E-TAC cycling. Charging was carried out at 1.43 V_{RHE} (a) or at 1.48 V_{RHE} (b) in 5M KOH aqueous solution at ambient temperature. The calculated Faradaic efficiency (eqn. S1) is based on the average current in each test presented in Figure 8 of the paper and the steady-state OER current at the same charging potential from Figure 7 of the article. The measured Faradaic efficiency is based on dissolved oxygen measurements, as shown in Figure 10 of the article.

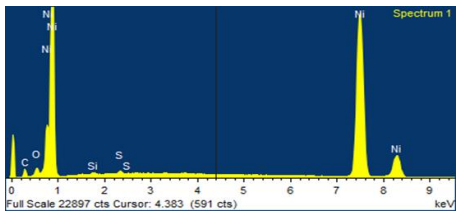Table S1: Compositional EDS analysis of nickel nanofibers after calcination (top) and after reduction (bottom).
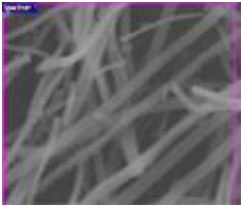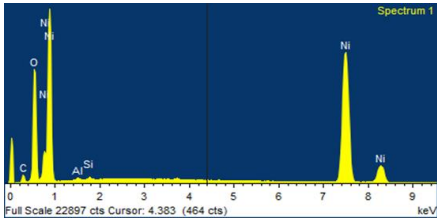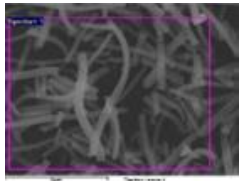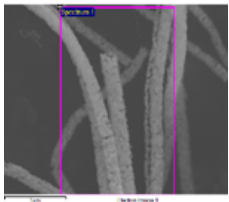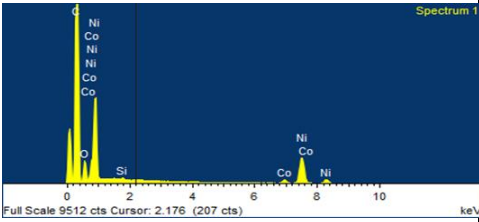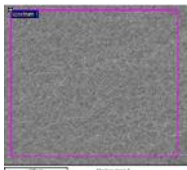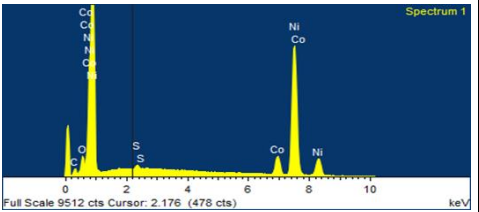
Sample	SEM micrograph	EDS spectrum	Composition (wt.%)	Composition (at. %)
Calcinated NiO fibers			Ni: 78.49% O: 21.51%	Ni: 49.86% O: 50.14%
Reduced Ni fibers			Ni: 98.67% O: 1.33%	Ni: 95.29% O: 4.71%

Table S2: Compositional EDS analysis of cobalt-doped nickel nanofibers after calcination and reduction.

Sample	SEM micrograph	EDS spectrum	Composition (wt.%)	Composition (at. %)
Cobalt-doped Ni fibers (reduced)			Ni: 87.46% Co: 10.6% O: 1.93%	Ni: 83.21% Co: 10.05% O: 6.74%
Cobalt-doped Ni fibers (reduced)			Ni: 89.31% Co: 9.33% O: 1.35%	Ni: 86.23% Co: 8.98% O: 4.80%

Supplementary references

1.   Recemat BV Cell Material Engineering. Nickel foam datasheet. (2019). Available at: http://www.metalfoam.nl/wp-content/uploads/2019/04/datasheet_nickel.pdf.

2.   Lasia, A. & Rami, A. Kinetics of hydrogen evolution on nickel electrodes. *J. Electroanal. Chem. interfacial Electrochem.* **294**, 123–141 (1990).

3.   Dotan, H. *et al.* Decoupled hydrogen and oxygen evolution by a two-step electrochemical-chemical cycle for efficieny overall water splitting. *Nat. Energy* **4**, 786–795 (2019).